Department of Micro- and Nanosciences

Approaches for optimizing light emitting diode structures based on III-N materials

Pekka Törmä

Aalto University

DOCTORAL DISSERTATIONS

Aalto University publication series
DOCTORAL DISSERTATIONS 27/2011

Approaches for optimizing light emitting diode structures based on III-N materials

Pekka Törmä

Doctoral dissertation for the degree of Doctor of Science in Technology to be presented with due permission of the School of Electrical Engineering for public examination and debate in the great hall in the Micronova building at the Aalto University School of Electrical Engineering (Espoo, Finland) on the 13th of May 2011 at 12 o'clock.

Aalto University
School of Electrical Engineering
Department of Micro- and Nanosciences

Supervisor
Prof. Markku Sopanen

Instructor
Dr. Tech. Sami Suihkonen

Preliminary examiners
Prof. Michal Leszczynski, Center for High Pressure Research of PASC, Warsaw, Poland
Prof. Micrea Guina, Optoelectronics Research Centre, Tampere University of Technology, Finland

Opponent
Assoc. Prof. Beata Kardynal, DTU Fotonik, Denmark

Aalto University publication series
DOCTORAL DISSERTATIONS 27/2011

ISBN 978-952-60-4082-0 (pdf)
ISBN 978-952-60-4081-3 (printed)
ISSN-L 1799-4934
ISSN 1799-4942 (pdf)
ISSN 1799-4934 (printed)

Aalto Print
Helsinki 2011

The dissertation can be read at http://lib.tkk.fi/Diss/

Aalto University

Abstract

Aalto University, P.O. Box 11000, FI-00076 Aalto www.aalto.fi

Author
Pekka Törmä

Name of the doctoral dissertation
Approaches for optimizing light emitting diode structures based on III-N materials

Publisher School of Electrical Engineering

Unit Department of Micro- and Nanosciences

Series Aalto University publication series DOCTORAL DISSERTATIONS 27/2011

Field of research Optoelectronics

Manuscript submitted 30 May 2010 **Manuscript revised** 4 March 2011

Date of the defence 13 May 2011 **Language** English

☐ **Monograph** ☒ **Article dissertation (summary + original articles)**

In this thesis fabrication and properties of light emitting diode (LED) structures based on III-N materials were studied. LED structures were grown by metal-organic vapor phase epitaxy (MOVPE). Especially increasing the light extraction efficiency (LEE) by using modified sapphire substrates was investigated. Optimization of InGaN/GaN and InGaN/InAlGaN multiple quantum well (MQW) structures was studied to improve internal quantum efficiency (IQE) of the LEDs. Electron blocking layer (EBL) was developed to increase carrier confinement into the active MQW region. The samples were characterized by x-ray diffraction (XRD), atomic force microscopy (AFM), scanning electron microscopy (SEM), photoluminescence (PL) and electroluminescence (EL) measurements.

Roughening and periodic patterning of the sapphire substrates were investigated in order to improve LEE. Significant improvements were achieved in LED performance with these methods. Also GaN material quality on patterned sapphire substrates (PSSs) was studied. It was found that using of PSSs enables reduction of threading dislocation (TD) density in the GaN layer. However, the effect on the LED performance caused by improved material quality was insignificant compared to the effect caused by improved LEE.

Various MOVPE processes were also evaluated for growth of InGaN/GaN MQW structures. Smooth surface morphology of the MQW stack was achieved by introducing a small amount of H2 during the MOVPE growth of the GaN barrier layers. The homogeneity between the quantum wells was improved by inserting an InGaN underneath layer. Quaternary InAlGaN layers were investigated and InGaN/InAlGaN MQW structures for near-UV emission were presented. IQE of InGaN/InAlGaN MQW structures was found to be sensitive to the InAlGaN barrier layer composition and the strain state of the structure.

Finally an AlGaN EBL for better carrier confinement is presented. It was found that the thickness and optimal Mg doping significantly affect the functionality of the EBL. A significant improvement in the LED performance was achieved by inserting an optimized AlGaN EBL into the LED structure.

Keywords LED, MOVPE, III-N materials, modified sapphire substrates

ISBN (printed) 978-952-60-4081-3 **ISBN (pdf)** 978-952-60-4082-0

ISSN-L 1799-4934 **ISSN (printed)** 1799-4934 **ISSN (pdf)** 1799-4942

Location of publisher Espoo **Location of printing** Helsinki **Year** 2011

Pages 123 **The dissertation can be read at** http://lib.tkk.fi/Diss/

Tekijä
Pekka Törmä

Väitöskirjan nimi
Approaches for optimizing light emitting diode structures based on III-N materials

Julkaisija Sähkötekniikan korkeakoulu

Yksikkö Mikro- ja Nanotekniikan laitos

Sarja Aalto University publication series DOCTORAL DISSERTATIONS 27/2011

Tutkimusala Optoelektroniikka

Käsikirjoituksen pvm 30.05.2010 **Korjatun käsikirjoituksen pvm** 04.03.2011

Väitöspäivä 13.05.2011 **Kieli** Englanti

☐ **Monografia** ☒ **Yhdistelmäväitöskirja (yhteenveto-osa + erillisartikkelit)**

Tiivistelmä

Väitöskirjassa tutkittiin III-N materialiaaliyhdisteisiin pohjautuvia valoa emittoivia diodi rakenteita (LED-rakenteita) ja näiden rakenteiden valmistusta. Erityisesti keskityttiin parantamaan valon ulostulotehokkuutta modifiomalla alustakiteenä käytettäviä safiirisubstraatteja. LED-rakenteet valmistettiin metallo-orgaanisella kaasufaasiepitaksialla (MOVPE). Työssä tutkittiin myös LED-rakenteen sisäisen hyötysuhteen parantamista optimoimalla käytettäviä InGaN/GaN- ja InGaN/InAlGaN-kvanttikaivorakenteita. Lisäksi työssä kehitettiin elektronienpysäytyskerros (EBL-kerros) keskittämään varauksenkuljettajat tehokkaammin kvanttikaivoihin. Tutkimuksessa käytettiin röntgendiffraktio-, atomivoimamikroskopia-, pyyhkäisyelektronimikroskopia- fotoluminesenssimittaus- ja elektroluminesenssimittausmenetelmiä.

Työssä tutkittiin safiirisubstraattien karhentamista ja säännöllistä kuviointia valon ulostulotehokkuuden parantamiseksi. Näiden menetelmien avulla saavutettiin huomattavia parannuksia LED-rakenteen tehokkuudessa. Lisäksi tutkittiin kuvioidun safiirisubstraatin käytön vaikutusta sen päälle valmistettavan GaN-kerroksen laatuun. Kuvioitujen safiirisubstraattien käytön havaittiin vähentävän GaN-kerroksessa esiintyviä kidevirheitä. Materiaalin laadun vaikutus LED-rakenteen toimintaan oli kuitenkin vähäinen verrattuna parantuneen ulostulotehokkuuden vaikutukseen.

Väitöskirjassa tutkittiin myös MOVPE-prosessien vaikutusta InGaN/GaN-kvanttikaivorakenteiden. Tasainen pinnan morfologia saavutettiin käyttämällä vetyä GaN-vallien valmistuksen aikana. InGaN/GaN-kvanttikaivojen toimintaa parannettiin lisäämällä rakenteeseen InGaN-alustakerros, joka paransi kvanttikaivojen keskinäistä homogeenisuutta. Lähi-UV-alueella toimivia LED-rakenteita varten tutkittiin InGaN/InAlGaN-kvanttikaivorakenteita. Sisäisen hyötysuhteen havaittiin riippuvan InAlGaN-vallien kompositiosta ja rakenteessa esiintyvästä jännityksestä.

Työssä kehitettiin lisäksi AlGaN-EBL keskittämään varauksenkuljettajat paremmin kvanttikaivoihin. Rakenteen toimivuuden kannalta AlGaN-kerroksen Mg-seostuksella ja paksuudella havaittiin olevan merkittävä vaikutus. LED-rakenteen toiminnassa saavutettiin huomattava parannus lisäämällä siihen optimoitu AlGaN-EBL.

Avainsanat LED, MOVPE, III-N materiaalit, modifioidut safiirisubstraatit

ISBN (painettu) 978-952-60-4081-3 **ISBN (pdf)** 978-952-60-4082-0

ISSN-L 1799-4934 **ISSN (painettu)** 1799-4934 **ISSN (pdf)** 1799-4942

Julkaisupaikka Espoo **Painopaikka** Helsinki **Vuosi** 2011

Sivumäärä 123 **Luettavissa verkossa osoitteessa** http://lib.tkk.fi/Diss/

Preface

The work done for this thesis has been carried out in the Department of Micro and Nanosciences at Helsinki University of Technology (TKK), nowadays Aalto University, during 2006-2009. I want to express my gratitude for financial support and funding of my thesis to the Graduate school of modern optics and photonics, OptoGaN Oy, the Finnish Funding Agency for Technology and Innovation (TEKES), Multidisciplinary Institute of digitalization and Energy (MIDE), the Finnish Foundation for Technology Promotion, the Väisälä Fund, Jenny and Antti Wihuri Foundation, and Walter Ahlström Foundation.

I want to thank Professor Markku Sopanen for his work as a supervisor of the thesis and Professor Harri Lipsanen for opportunity to work at the Department of Micro and Nanosciences. I want to thank also Dr. Maxim Odnoblyudov and Dr. Vlasdislav Bougrov from OptoGaN Group for support and collaboration during the previous years.

Great thanks and high fives go to official THY research team members Dr. Sami Suihkonen, the instructor of the thesis, Mr. Olli Svensk, Mr. Muhammad Ali and Mr. Sakari Sintonen. I can honestly say that working in some other group would have been boring compared to you guys. Dr. Outi Reentilä and Mr. Pasi Kostamo have been important persons before and during my thesis as a colleagues and friends. I am also grateful to Dr. Lauri Knuuttila and Ms. Annette Czodrowski for motivation and friendship during the last slow motion year of my thesis.

My parents and my sister have deserved great thanks for their support during all these years of education. Last but not least thing I want to thank Leena the wife for her love, warmness and understanding.

Landshut, 26.03.2011

Pekka Törmä

Contents

List of publications

This thesis consists of an overview and of the following publications which are referred to in the text by their Roman numerals.

I P. T. Törmä, O. Svensk, M. Ali, S. Suihkonen, M. Sopanen, M. A. Odnoblyudov, and V. E. Bougrov, *Maskless roughening of sapphire substrates for enhanced light extraction of nitride based blue LEDs*, Solid-State Electronics **53**, 166 (2009).

II P. T. Törmä, M. Ali, O. Svensk, S. Sintonen, P. Kostamo, S. Suihkonen, M. Sopanen, H. Lipsanen, M. A. Odnoblyudov, and V. E. Bougrov, *An investigation of structural properties of GaN films grown on patterned sapphire substrates by MOVPE*, Physica B: Condensed Matter **404**, 4911 (2009).

III P. T. Törmä, M. Ali, O. Svensk, S. Suihkonen, M. Sopanen, H. Lipsanen, M. Mulot, M. A. Odnoblyudov, and V. E. Bougrov, *InGaN-Based 405 nm near-ultraviolet light emitting diodes on pillar patterned sapphire substrates*, CrystEngComm **12**, 3152 (2010).

IV S. Suihkonen, T. Lang, O. Svensk, J. Sormunen, P. T. Törmä, M. Sopanen, H. Lipsanen, M. A. Odnoblyudov and V. E. Bougrov, *Control of the morphology of InGaN/GaN quantum wells grown by metalorganic chemical vapor deposition*, Journal of Crystal Growth **300**, 324 (2007).

V P. T. Törmä, O. Svensk, M. Ali, S. Suihkonen, M. Sopanen, M. A. Odnoblyudov, and V. E. Bougrov, *Effect of InGaN underneath layer on MOVPE-grown InGaN/GaN blue LEDs*, Journal of Crystal Growth **310**, 5162 (2008).

VI S. Suihkonen, O. Svensk, P. T. Törmä, M. Ali, M. Sopanen, H. Lipsanen, M. A. Odnoblyudov and V. E. Bougrov, *MOVPE growth and characterization of InAlGaN films and InGaN/InAlGaN MQW structures*, Journal of Crystal Growth, **310**, 1777 (2008).

VII M. Ali, S. Suihkonen, O. Svensk, P. T. Törmä, M. Sopanen, H. Lipsanen, M. A. Odnoblyudov and V. E. Bougrov, *Study of Composition Control and Capping of MOVPE Grown InGaN/$In_xAl_yGa_{1-x-y}N$ MQW Structures*, physica status solidi (c) **5**, 3020 (2008).

VIII O. Svensk, P. T. Törmä, S. Suihkonen, M. Ali, H. Lipsanen, M. Sopanen, M. A. Odnoblyudov, and V. E. Bougrov, *Enhanced electroluminescence in 405 nm InGaN/GaN LEDs by optimized electron blocking layer*, Journal of Crystal Growth, **310**, 5154 (2008).

Author's contribution

The author has written the manuscripts and designed the experiments for publications I, II, III and V.

The author has performed the major part of the epitaxial sample fabrication, sample processing, data collection and data analysis for publications I, II, III and V.

The author has contributed to the design of experiments, performed parts of the epitaxial sample fabrication, and data analysis and assisted in writing of the manuscript for publication VIII.

The author has contributed to the design of experiments and performed parts of the epitaxial sample fabrication for publications IV, VI and VII.

List of Abbreviations

AFM	atomic force microscopy
AlN	aluminum nitride
CCS	close coupled showerhead
CBM	conduction band minimum
CPs	concentration points
CS	conventional sapphire
EBL	electron blocking layer
ELOG	epitaxial lateral overgrowth
EL	electroluminescence
EPD	etch pit density
FWHM	full width at half maximum
GaN	gallium nitride
GI	growth interruption
HS	holes on the sapphire
HVPE	hydride vapor phase epitaxy
InN	indium nitride
ICP-RIE	inductive coupled plasma reactive ion etching
IQE	internal quantum efficiency
I-V	current-voltage
LC	lattice constant
LED	light emitting diode
LEE	light extraction efficiency
LDPS	low density pillar structure
LT	low temperature
MBE	molecular beam epitaxy
MFCs	mass flow controllers
MOVPE	metal organic vapor phase epitaxy
MQW	multi quantum well
MSM	multistep method
NRCs	nonradiative recombination centers
PE	pendeo epitaxy
PL	photoluminescence
PSSs	patterned sapphire substrates
PS	pillars on the sapphire
QCSE	quantum-confined Stark effect
QWs	quantum wells
RT	room temperature

SEM	scanning electron microscopy
SIMS	secondary ion mass spectroscopy
TDs	threading dislocations
TD	threading dislocation
TMA	trimethylaluminium
TMG	trimehtylgallium
TMI	trimethylindium
UL	underneath layer
UV	ultra violet
VBM	valence band maximum
XRD	X-ray diffraction

1 Introduction

Optoelectronics, as may be understood from it's name, is a research area examining the interaction between light and electrical material. Light can be created or detected electrically with semiconductor based optoelectronic components. Often these components also have a key role in various applications in our everyday life including optical telecommunication, data storage, solar cells etc. Light emitting diode (LED) is a basic semiconductor optoelectronic device. Even still it has a significant role in the battle against global warming. Even thought LEDs have quite a narrow spectrum for illumination, white light can be created by exciting white phosphors with blue or ultra violet (UV) LED light sources. LEDs have several significant benefits including low energy consumption, long life time, affordable price, and customable color spectrum. These properties make LEDs the most potential choice for next generation general lighting and illumination after the compact fluorescent lamps [1].

The LED was introduced for the first time in 1962 [2]. However, it took decades before efficient materials were found for blue and UV emitters operating at short wavelengths. Compound semiconductors based on II-VI elementals have been studied extensively for this purpose. However, a breakthrough came finally from III-N material system. Several major technical innovations during the 1990's launched a rapid development of short wavelength LEDs and laser diodes [3]. Those key inventions were awarded by Millennium prize in 2006. Currently III-N materials are considered to be the best choice for environmental-friendly solid-state lighting. Although efficiency and material quality of the III-N emitters has dramatically increased due the extensive research, there still exist many challenges reducing the operating performance of the III-N based LEDs. Growth of high quality quantum well structures for quantum confinement of carriers is complicated for blue LEDs and is even more challenging for UV LEDs [4]. In the III-N based LEDs operating in the UV range issues related to crystal quality such as dislocations become a serious limiting factor for efficiency. Efficient carrier injection and confinement into active region is also a critical issue. Finally efficient light extraction is required to guide created light out of the LED structure.

In this thesis some of the problems limiting the LED performance are addressed, and approaches for optimizing the blue and UV-LEDs for more efficient operation are presented. The structure of this thesis is as follows. Chapter 2 reviews the III-N

material fundamentals needed for understanding the operation of the LED based on on this material system. Chapter 3 outlines the main experimental methods used. Chapter 4 discusses the general era of the LEDs, the epitaxial structure of the III-N LEDs and the critical issues related to III-N LED performance. Chapter 4 also introduces how the publications I-VIII are related to III-N LED structures. The results of the work are reviewed in chapter 5. Finally a summary of the main results of this thesis is given in chapter 6. The publications of this dissertation are attached at the end of this thesis.

2 Fundamentals of III-N materials

This chapter presents a brief introduction to the properties and nature of the III-N semiconductor material family.

2.1 Crystal structure

A solid state material can exist in amorphous state, where the positions of the atoms lack long-range ordering. A crystal is the other form for solid state material, where the atoms are located in their exact positions which follow a strict periodicity. The unique properties of the semiconductors follow from their crystalline nature. There are several different known crystalline structures. However, group III-N materials can crystallize only in two of these forms, namely wurtzite and zinc blende lattice [5]. Because all the samples fabricated for this work have wurtzite crystal structure, the following text reviews only that structure while the other crystal structures are omitted.

In the hexagonal wurtzite lattice, shown in Fig. 2.1, atoms are tetrahedrally bonded to their neighbors. Lattice parameters c, a and u define a unit cell and the exact place of any individual atom can be calculated from them. The lattice constant c defines the distance between two identical hexagonal lattice planes while the lattice parameter a is the spacing of atoms in the hexagonal lattice plane. The last lattice parameter u is dimensionless defining the bond length along the c-direction and distortion of the unit cell. In the wurtzite gallium nitride (GaN) unit cell the neighboring lattice planes contain only one element, either Ga or N atoms. The relative positioning of the atoms in one lattice plain is such that they form a hexagon. Also indium nitride (InN), aluminum nitride (AlN) and their ternary and quaternary alloys with GaN can crystallize into hexagonal wurtzite form. The only difference to the GaN lattice is that the Ga atoms are either completely or partly replaced by the other group III atoms. However, changing one element with another naturally changes the lattice parameters, because of the different atom sizes. The lattice constants for III-N materials GaN, InN and AlN are given in Table 2.1 [6].

One important issue of GaN films is that they have significant polarization properties. The total polarization is the sum of spontaneous and piezoelectric

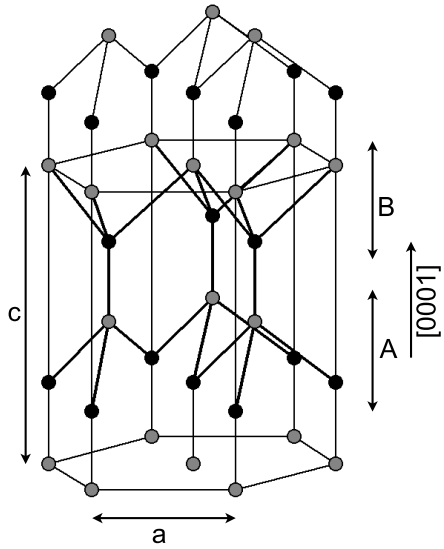

Figure 2.1. Unit cell of hexagonal wurtzite GaN. In Ga-polar film black color depicts N atoms and gray Ga atoms. In N-polar gray color depicts N atoms and black Ga atoms [7].

Table 2.1. Lattice constants c, a and u for GaN, InN and AlN [8].

Lattice constant	**GaN**	**InN**	**AlN**
c (Å)	5.185	5.718	4.982
a (Å)	3.189	3.544	3.112
u	0.3768	0.3790	0.3819

polarization in the absence of external fields. The origins of the spontaneous polarization can be found in the strong ionic nature of the III-N bond. The structure of the wurtzite unit cell contains asymmetry between [0001] and [000$\bar{1}$] directions. This is called an internal polarity of the film defined by the group III-N bond direction aligned parallel to the c-axis. The GaN film is called as Ga-polar in the case of group III atoms forming the topmost atomic layer and N-polar in the opposite case (Fig. 2.1). GaN-films grown by MOVPE, as in this work, are known to be Ga-polar. The polarity affects the surface properties and the direction of the piezoelectric field in the III-N materials [9–11].

The existence of the piezoelectric polarization is caused by the reason, that GaN lacks inversion symmetry and exhibits piezoelectric effects when strained along $\langle 0001 \rangle$ direction. Piezoelectric coefficients in III-N materials are almost an

order of magnitude higher than in many conventional III-V semiconductors. The piezoelectric effect has two components due the lattice mismatch and thermal strain between the substrate and the epitaxial film [5].

2.2 Electronic band structure

In the crystal structure the periodic potential affects electron energy states. This potential causes splitting of the electron states into energy bands. Forbidden electron energy states called a band gap exist between these bands. Valence band is the highest energy band containing electrons at 0 K temperature. The lowest empty energy band is called a conduction band. Depending on the band structure semiconductors can be divided into direct and indirect band gap semiconductors. In direct band gap semiconductors, such as GaN, the conduction band minimum (CBM) and the valence band maximum (VBM) are located at the same electron wave vector marked with $\overline{k}$. This property makes an optical transition between CBM and VBM significantly more probable than in the indirect case, where a change in the electron momentum is required in addition to the conservation of energy [12]. Fig. 2.2 shows the calculated band structure of hexagonal wurtzite GaN near the band gap.

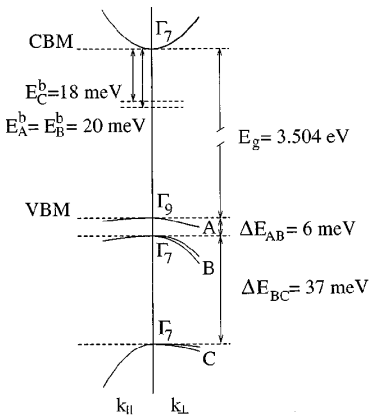

Figure 2.2. Electronic band structure of hexagonal wurtzite GaN near the $\bar{k}$-space point $\bar{k}$=0 [13].

The direct band gap and the sizes of the energy gaps of the III-N materials AlN, GaN and InN are the major reasons behind the huge interest towards them. Fig. 2.3 shows the band gap versus lattice constant a for III-N materials. In theory, alloying of III-N in ternary or quaternary form can be used to tune the band gap from deep-UV 6.2 eV of pure AlN to infrared 0.7 eV of pure InN. However, the

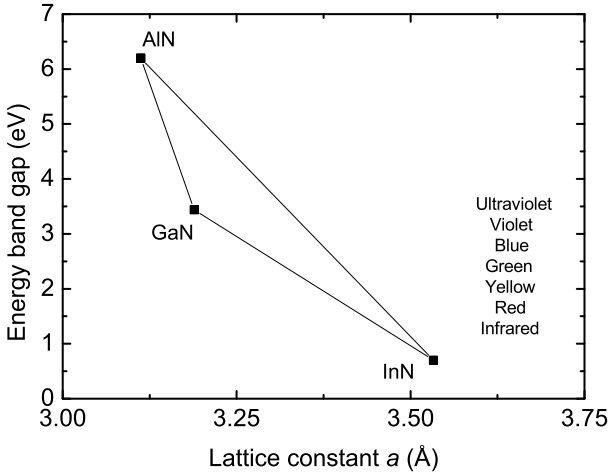

Figure 2.3. Band gaps and lattice constants of AlN, GaN and InN as a function of lattice constant a [7].

challenges in the growth process due the different optimum growth conditions of In and Al containing alloys practically limit the wavelength range of GaN based LEDs from UV to green [4].

The ternaries InGaN and AlGaN are the most common group III-N ternary alloys used in a number of applications. The band gap of ternary compound ABC can be calculated from [12]

$$E_g(A_xB_{1-x}C) = xE_g(AC) + (1-x)E_g(BC) - x(1-x)C_{ABC}, \tag{2.1}$$

where C_{ABC} is a bowing parameter of the ternary ABC, and $E_g(AC)$ and $E_g(BC)$ are the band gaps of the binaries AC and BC, respectively. In the case of quaternary compound such as $In_xAl_yGa_{1-x-y}N$ the band gap energy can be written in a little bit more complex form [14]

$$E_g(x,y) = xE_{g,InN} + yE_{g,AlN} + (1-x-y)E_{g,GaN} - b_{Al}y(1-y) - b_{In}x(1-x). \tag{2.2}$$

The bowing parameters related to Al and In composition are denoted by b_{Al} and b_{In}, respectively. The band gap energy of $Al_yGa_{1-y}N$ can be modeled with a static bowing parameter b_{Al} [15, 16]. In-containing alloys are more complex to model, because the bowing parameter b_{In} depends strongly on the In and Al content [14, 17].

2.3 Substrate materials

Because single crystal GaN substrates with reasonable size and price are not widely available, growth of III-N materials is typically based on heteroepitaxy. Many problems that have slowed down the progress of III-N semiconductors can be traced back to the lack of an ideal substrate. Lattice mismatch is largely responsible for stacking faults and threading dislocations (TDs). Difference in thermal expansion coefficients causes strain and may crack the epilayer on cooling. During the years GaN has been grown on various substrates including Si, NaCl, GaP, InP, W, ZnO, $MgAl_2O_4$, SiC (4H and 6H) and sapphire Al_2O_3 (c-, a-, m- and r-planes). The most promising results so far have been obtained on SiC and sapphire. SiC has an advantage of small lattice mismatch with GaN. It also has a good thermal conductivity which is beneficial for device operation and lifetime. However, due the high price of SiC substrates, sapphire is the most widely used substrate for GaN epitaxy. Sapphire is available with large area and high crystal quality at low cost. Sapphire is also transparent at visible wavelengths and has good thermal and chemical stability [5, 18]. The lattice parameters and thermal characteristics of the most widely studied substrates for III-N material growth are shown in Table 2.2.

Table 2.2. Lattice parameters and thermal characteristics of the most widely studied substrates for III-N material growth and their lattice mismatch with GaN. Modified from [5].

	Conventional			Matched a	Therm. cond.	$\Delta a/a$, $\Delta c/c$	
Crystal	a (Å)	b (Å)	c (Å)	(Å)	($\frac{W}{cmK}$)	(10^{-6} K^{-1})	Mismatch
AlN (hex.)	3.104	-	4.966	3.104	3.2	4.2, 5.3	-2.7 %
GaN (hex.)	3.189		5.185	3.19	2.3	5.59, 3.17	0 %
Al_2O_3 (hex.)	4.758		12.991	2.747	0.3-0.5	7.5, 8.5	49 % (16 %)
4H-SiC (hex.)	3.073		10.053				-3.63 %
6H-SiC (hex.)	3.0817		15.1123	3.0817	4.9	4.2, 4.68	-3.63 %
ZnO (hex.)	3.2496		5.2065	3.2496	0.3-0.4	4.75, 2.9	1.9 %
Si (cubic)	5.4301				1.5	3.59	

On a c-plane sapphire the wurtzite GaN lattice is rotated 30^o relative to the substrate crystal lattice to minimize stress resulting in a 16 % lattice mismatch instead of 49 % mismatch between the original lattice parameters (Table 2.2). In this thesis all the samples were grown on c-plane (0001) sapphire. However, for some of the

samples sapphire substrates were modified with surface patterning or roughening by chemical wet etching. The patterning process and the epitaxial growth process on patterned sapphire substrates are discussed in more detail in sections 5.1 and 5.2, respectively.

3 Experimental

In this chapter the main experimental fabrication and characterization methods used in this thesis are presented.

3.1 Metalorganic vapor phase epitaxy

Epitaxy is a crystal growth method where the growing layers copy the crystal structure of the underneath layers. In optoelectronic components the final structure commonly consists of several different epitaxial semiconductor layers grown on the substrate. Thickness, material combination and crystal quality directly affect the component performance.

Metal organic vapor phase epitaxy (MOVPE) together with molecular beam epitaxy (MBE) are the main methods for fabricating compound semiconductor structures. Low dimensional structures with sharp interfaces and good composition control can be achieved by both methods. However, there is a fundamental difference how the atoms are delivered to the substrate between these methods. MBE has an ultra high vacuum chamber where elemental sources are evaporated to the heated substrate. In MOVPE atoms of the layer are provided from metalorganic precursor vapors delivered on the heated substrate using commonly either H_2 or N_2 as a carrier gas.

The growth process in MOVPE is defined by thermodynamics, kinetics, hydrodynamics and mass transport. Thermodynamics describe the driving forces making chemical reactions possible. Rate of the reactions is defined by kinetics. Hydrodynamics describe precursor material transport to the reaction interface. Mass transport determines diffusive transport of the species through the reaction interface, making self organization of the atoms in the epitaxial crystal growth possible [19].

Composition, thickness and quality of the grown layer are controlled in the MOVPE technique by growth parameters such as pressure, temperature, gas flow ratios, total gas flow and precursor materials. Typical examples of metalorganic precursors are trimehtylgallium (TMG), trimethylindium (TMI) and trimethylaluminium (TMA), which are commonly used as group III sources in the growth process of III nitride materials. Ammonia is the *de facto* choice for the group V nitrogen precursor.

The gas flow diagram of the MOVPE system used in this work is schematically represented in Fig. 3.1. Steel cylinders containing the liquid metalorganic precursors are kept in temperature controlled baths. When carrier gas flows through the cylinder it is saturated with the metalorganic material. The amount of saturated vapors is determined by the vapor pressure of the precursor, which is extremely sensitive to the temperature of the cylinder. The gas flows are guided with electronic valves and mass flow controllers (MFCs) into the reactor chamber. The group III and V sources are guided in separate pipelines to the reactor to avoid harmful pre-reactions. The fast switching of gas flows to or past the reactor allows the growth of low dimensional structures such as quantum wells (QWs) with sharp interfaces.

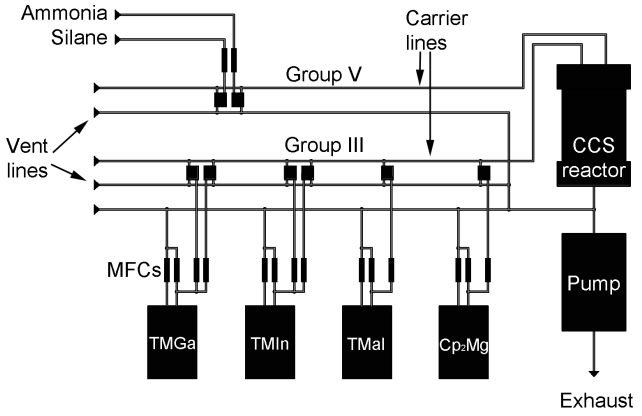

Figure 3.1. A simplified diagram of the CCS MOVPE system used in this work.

A detailed schematic of the close coupled showerhead (CCS) reactor manufactured by Thomas Swan Scientific Equipment is illustrated in Fig. 3.2. A benefit of the CCS reactor is that the precursors of the elemental group III and V are kept separate as long as possible and they are mixed only very next to the substrate surface. This reduces possible pre-reactions of the precursors. The reaction chamber has positions for three 2" wafers. A SiC-coated graphite susceptor is rotated during the growth process to ensure a homogeneous precursor flow on the substrates. The heating of the susceptor is done by underneath resistive tungsten coils having a temperature range from room temperature to 1200 ^{o}C. In situ reflectance monitoring (Fig. 3.3) in normal incidence at a wavelength of 635 nm is used to monitor film growth in real time. In situ technique offers essential information about growth rate and surface roughness of the films [6, 20, 21]. It is also very important tool to control nucleation in the beginning of GaN growth on sapphire [3, 7, 21].

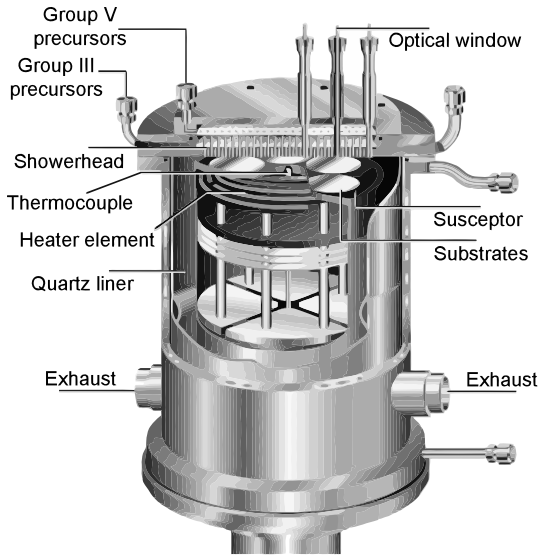

Figure 3.2. Structure of the CCS reactor in the MOVPE system used in this thesis [22].

3.2 X-Ray diffraction

X-ray diffraction (XRD) is an elegant non destructive method to characterize the composition, thickness and interface quality of each layer of the epitaxially grown semiconductor material. In the simplest picture X-ray diffraction from crystalline lattice planes can be described by the Bragg's law

$$2d \sin\theta = n\lambda, \tag{3.1}$$

where d is a separation between different lattice planes, θ is the angle between the diffracted beam and the diffracting lattice planes, n is an integer and λ is the wavelength. The separation d depends on the lattice constant which itself depends on the layer composition, strain and relaxation state. Thus, these layer parameters have effect on the diffraction measurement. Also the layer thicknesses determine the periodicity of the diffraction pattern.

The most convenient way to analyze XRD-measurements, which was also used in this thesis, is to simulate the theoretically calculated diffraction pattern and fit it together with the measured diffraction pattern by sophisticated algorithms. Theoretical calculation is based on dynamic diffraction theory and is related to

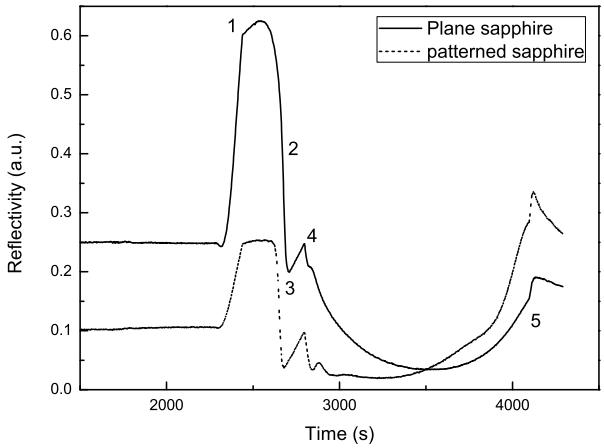

Figure 3.3. Example in situ reflectance curves from growth runs on plane and patterned sapphire substrates. Numbers refer to the following phases of growth 1) low temperature nucleation layer, 2) nucleation island formation, 3) partial exposure of the sapphire surface, 4) starting of the high temperature 3D GaN growth and 5) coalescence of the 3D islands in the beginning of the GaN growth process.

Takagi-Taupin equations [23–25]. Downside of the XRD measurement method is that the results are not unique. Several combinations of parameters may give sufficient fit. Differences caused by the change of one parameter are straightforward to observe when the other parameters in the structure can be fixed. Precise determination of the layer thicknesses and compositions from complex semiconductor structures demands combination of other measurement methods together with XRD [26].

A Philips X'Pert high resolution X-ray diffraction system was used to characterize the samples for this thesis. The basic measurement setup is illustrated in Fig. 3.4. For reducing the divergence of the incident beam a X-ray mirror is located between the X-ray tube and the monocromator. The Cu-$K\alpha_1$ line ($\lambda = 1.541$ Å) is selected by using a four crystal germanium monocromator. The movable and rotatable sample stage provides freedom to select diffraction from different lattice planes over the complete half sphere. The analyzer reduces the diffracted beam intensity but enhances the measurement resolution significantly.

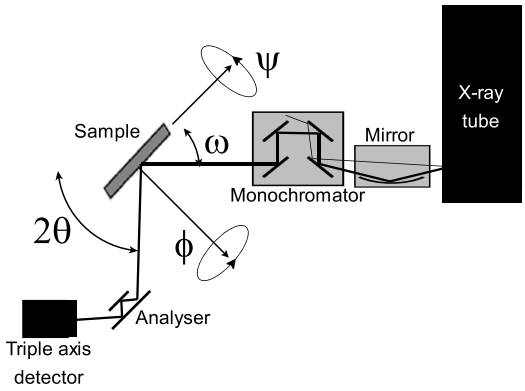

Figure 3.4. Schematic illustration of the XRD measurement setup.

3.3 Scanning electron microscopy

Scanning electron microscopy (SEM) is maybe the most elegant characterization and fabrication method for nanoscale structures. SEM gives a direct image, similar to that from normal microscope, of the scanned sample. However, the resolution of SEM is limited by the electron de Broglie wavelength instead of visible light wavelengths. Thousands of times smaller wavelength compared to the visible light significantly increases the resolution limit caused by diffraction. This leads to nanometer scale resolution depending on the conductivity of the samples, and the hardware or software capability of the system [27].

A schematic illustration of the SEM imaging process is shown in Fig. 3.5. An electron beam is accelerated in vacuum by voltage typically in the range of 1-20 kV and focused to very narrow spot, which is then scanned over the sample. Secondary electrons emitted by the atoms near the spot are collected by a detector. Detector current is amplified and the final image is generated from the combination of the detector current and the beam spot position information. Back-scattered electrons can be used for imaging instead of secondary electrons. Because the amount of electrons collected by the detector is strongly depended on the beam angle of incidence SEM offers more information about 3D nature of the sample compared to the conventional microscope. In this thesis Zeiss Supra Forty SEM was used for structural characterization of the samples.

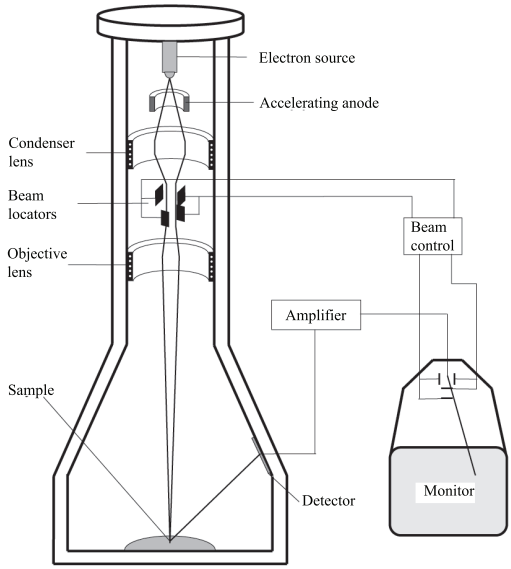

Figure 3.5. Schematic principle of the electron optics of a SEM.

3.4 Atomic force microscopy

In atomic force microscopy (AFM) an extremely sharp tip attached to the cantilever scans the sample surface. The method is nondestructive and a fast way to measure morphological properties of surfaces in the nm scale. The schematic illustration of the AFM operating principle is shown in Fig. 3.6. A sharp tip interacts with the surface of the investigated material. As the sample is moved Coulombic or van der Waals forces between the sample surface and the tip cause bending of the flexible cantilever attached to the tip. The bending of the cantilever is detected optically by using a reflected laser beam and a dual-photodetector. The vertical distance between the sample and the tip is kept constant by a vertical piezoelectric sample actuator using a feedback from the dual-photodetector. The feedback information data is collected and a computer converts the data to height information about the surface morphology.

In this thesis the fabricated nitride films were characterized by NTegra and Nanoscope IIIe atomic force microscopes using contact and semi-contact modes. The vertical resolution of these systems is typically around 0.1 nm which makes imaging of individual atomic steps possible. The lateral resolution, which is typically in the range of few tens of nanometers, is limited by the type of the tip and the surface morphology of the imaged sample.

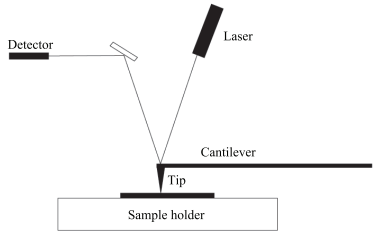

Figure 3.6. Schematic operating principle of the AFM measurement.

3.5 Optical spectroscopy

Photoluminescence (PL) is a sophisticated and fast non-destructive method to get information about the optical quality of semiconductor structures. In PL the carriers generated by absorbtion of photons recombine either radiatively or non-radiatively at the energy states near the band edges. The spontaneously emitted recombination light is collected and then analyzed by a spectrometer. The optical properties of LEDs and QW samples were characterized by both room temperature (RT) and low temperature (LT) PL. The PL spectra were measured by using a He-Cd laser (λ = 325 nm, power 20 mW) as an excitation source.

The internal quantum efficiencies (IQEs) of some samples were estimated from the total luminescence ratio of the PL measured at 300 K and 10 K (I_{300}/I_{10}). This determination is based on the principle that luminescence intensities and lifetimes are strongly dependent on temperature. At higher temperatures, non-radiative recombination is known to have a dominant effect. Carrier lifetime in InGaN QWs does not change anymore at temperatures below 25 K, meaning that non-radiative recombination is frozen, therefore, can be neglected [28].

Electroluminescence (EL) measurements at RT were also used to characterize LEDs. In the EL the basic principle is the same as in PL, but instead of photon excitation of carriers an external current source is used to transport carriers to the active region. For EL measurements two types of contacts were used. Soldering of 0.5 mm^2 metallic In contacts to the p- and n- layers on the LED wafers was a fast method for EL measurements. Also for more sophisticated EL measurements LED mesas having 440x440 μm^2 dimensions were manufactured from the epi-wafers. The n-contact region was defined by plasma etching in order to expose the n-GaN layer. A transparent conductive oxide was used in order to favor current spreading in the p-GaN layer. In the EL measurements individual chips on each wafer were probed. In both cases the EL spectra and the output power were collected by a spectrometer. The EL measurements were averaged from several separate measurements for improving the reliability of the measurement.

3.6 Sapphire etching chamber

Wet etching of the sapphire was done by a mixture of H_2SO_4:H_3PO_4 in the temperature range of 240-320 ^oC. The method gives the possibility to work with a simple apparatus and accessible reactives. However, the method has safety issues due to the usage of hot acids in this temperature range. Fig. 3.7 shows the etching chamber design for heating the chemicals during the etching. The chamber and the sample holder were made of vacuum compressed quartz. Creation of hot acid vapor during the process causes a demand of efficient vapor condensation and air exhaust to insulate people from the hazardous vapor. Etch rate of the sapphire can be increased by having a magnetic stir bar in the etching solution [29].

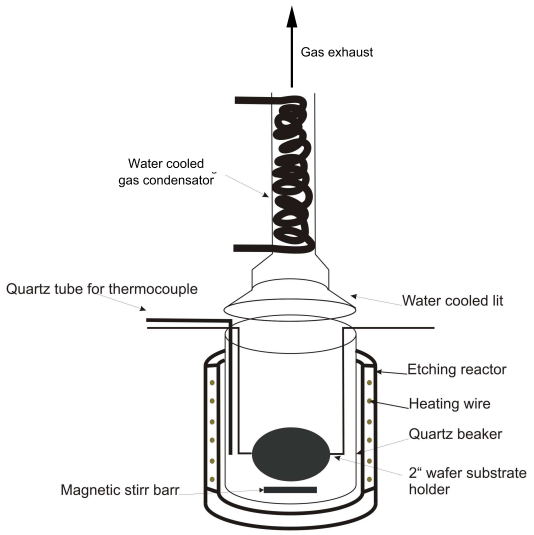

Figure 3.7. Schematic illustration of the sapphire wet etching chamber.

Temperature, time, solubility of the etching product, and acidity of the solution determine the sapphire etch rate. H_2SO_4 and H_3PO_4 are both known to dehydrate

to more acidic diacids upon heating based on the following reactions [30]

$$2H_3PO_4 \rightarrow H_4P_2O_7 + H_2O, T > 215^oC \tag{3.2}$$

$$2H_2SO_4 \rightarrow H_4S_2O_7 + H_2O \tag{3.3}$$

In the etching process Al_2O_3 molecules dissolve into the acids as Al^{3+} and acid molecules dissociate into their ionic species including mainly H^+, HSO_4^-, and SO_4^{2-} for H_2SO_4 , and H^+, $H_2PO_4^-$, HPO_4^{2-} and PO_4^{3-} for H_3PO_4. Below 300 ^{o}C the etch rate is limited by the surface reactions due to the exponential dependence of the temperature. H_2SO_4 and H_3PO_4 have different etching behavior because of their chemical nature. H_2SO_4 is much stronger acid than H_3PO_4 while conjugated phosphate anions are more nucleophilic than sulfate ions. The high reactivity of the phosphates towards aluminum means lower activation energy for the H_3PO_4 etching. However, the etch rate also depends strongly on pH causing the higher etch rate observed with stronger H_2SO_4 [29, 30].

H_2SO_4 etching of the c-plane sapphire does not preferentially etch at defect sites, therefore no pits are observed on the surface. However, deposition of insoluble reaction products occurs on the surface. Deposition rate of these products increases with temperature. Reaction products form a barrier layer preventing the reactant transport to the sapphire surface. Al^{3+} reacts with SO_4^{2-} to form a mixture of different phases of hydrous aluminum sulfate according to [30]

$$2Al^{3+} + 3SO_42- + xH_2O \rightarrow Al_2(SO_4)_3 \cdot xH_2O \tag{3.4}$$

Al_2O_3 is known to be able to form different phosphate related solid phases with H_3PO_4. The reaction between H_3PO_4 and Al_2O_3 is complex involving large number of possible reaction products and intermediate steps. However, in the H3PO4 etching of sapphire, there are no insoluble reaction products. Reaction products are considered to consist only soluble $Al(H_2PO4)_3$ and hydrous $AlPO_4$, which have a high solubility in H_3PO_4 [29, 30].

4 III-N LEDs

In this chapter a short overview of the typical epitaxial III-N LED structure is presented. The issues related to the LED efficiency including internal quantum efficiency (IQE) and light extraction efficiency (LEE) at the epitaxial and chip level are discussed.

4.1 Overview

Electric lighting forms approximately 19 % of the total global electricity consumption. Lighting is one of the biggest causes of greenhouse gas emissions with 1900 megatonnes of CO_2 (year 2005), which is not so often realized. This is equivalent to 70 % of the emissions that come from cars [31]. With this perspective there is an enormous demand for more environmental friendly lighting systems. The most probable choice for next generation of home and office lighting is the inorganic LEDs.

The major benefits of LEDs compared to conventional lighting fixtures are their energy efficiency, long life time and possibility to control the emission spectrum for any desired color [1]. LEDs introduce huge possibilities for energy saving, more maintenance-free and personally customable lighting fixtures for today and tomorrow while this technology penetrates deeper into the global markets [1, 31]. The luminous efficiency of the commercial white light LED sources are already in the level of 95 lm/W [32]. For a comparison luminous efficiency of the incandescent lamps and fluorescent tubes are 20 lm/W and 70 lm/W, respectively. Moreover, the theoretical limit of the LED efficiency in the ideal case is over 300 lm/W [33]. An another benefit of the LEDs is the color rendering index as high as 95/100 which makes them more capable to render natural colors for the human eye [32–34].

Inorganic LEDs have been used since their invention in 1962 as the ubiquitous little lights that indicate if our electronic equipment is on, if the battery of the fire detector is low, *etc* [2]. The first visible LEDs based on GaAsP were emitting in the red part of the spectrum [34]. A mass production of these LEDs was launched for the first time in 1968. The direct-indirect transitions and the high dislocation density decrease the brightness attainable with GaAsP LEDs. However, this material system is still

used as the standard choice for low brightness (LB) red LED applications such as indicators. Another material family introduced for LEDs also in the late 1960's is based on GaP. With suitable impurity doping this indirect band gap semiconductor can be used as an efficient source for red and green emission. Today, nitrogen doped GaP is the primary material for LB green emitters [31, 34].

AlGaInP material system, which was introduced for LEDs later compared to the GaAsP and GaP material systems, has been under development since 1985. AlGaInP LEDs has paved the way for red and amber LEDs to compete directly with conventional lighting technologies [34, 35]. High-power AlGaInP LEDs were the first LED devices that exceeded the luminous efficiency of most fluorescent bulbs [35].

The lack of suitable material system for efficient blue emitters limited the success of LED devices still in the beginning of 1990's. Since the first demonstration of high brightness InGaN based blue LED in 1993 [6], the development of semiconductor growth technology has rapidly increased in the field of applications including full color displays wherein several single to several millions of LEDs can be packaged together, traffic lights, automotive lighting scheme and general lighting. InGaN is a part of the III-N material family which is the only practical choice for fabrication of efficient inorganic LEDs from green to deep-UV range. These materials also have the main role in the LED-based general lighting, because the most cost effective way to produce white LEDs is to cover either blue or near-UV LED chip, represented in Fig. 4.1, with color converting phosphor [1, 6].

Currently there are two main factors limiting the fabrication of high power LEDs for general lighting. Green gap originates from the fact that efficiency of the InGaN QWs decreases with high In contents needed for green emission. Also other material families have low efficiency for producing green LEDs [31, 34]. Another issue is that InGaN based LEDs exhibit a serious fall-off in efficiency when the devices are operated at high current densities. Several reasons for this behavior have been suggested, such as electron overflow to p-side [36], defect related parasitic current [37], carrier overflow from localize states [38], potential barriers induced by piezoelectric polarization [39] and Auger-like recombination [40]. The scientific community is not unanious about the real reason for the efficiency droop.

4.2 Early stages of III-N materials

The first single crystal GaN on sapphire substrate was grown by hydride vapor phase epitaxy (HVPE) in 1969 [41]. It was also found that GaN has a direct band gap with the energy of 3.46 eV at RT [42]. This launched an increased interest towards the III-N materials. However, growing high quality GaN film was found to be challenging. Residual donors in GaN made producing of p-type GaN and

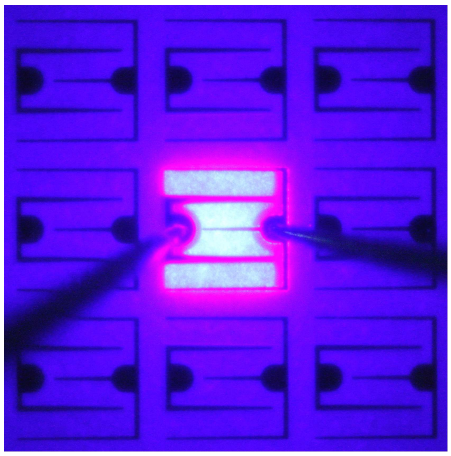

Figure 4.1. Optical microscope image of a near-UV LED-chip emitting at 405 nm emission peak wavelength, operating at low current level.

controlling of the conductivity of n-type GaN very difficult. Thus after few years the research activity in the III-N field cooled down [3].

During the early years GaN material study was done with HVPE and later also with MBE. However, growing the high quality GaN with reasonable uniformity stayed an unsolved challenge. A significant breakthrough in the III-N history was utilization of the MOVPE deposited LT-AlN buffer layer on the sapphire substrate for the reduction of interfacial free energy caused by the large thermal and lattice mismatch between GaN and sapphire. The world's first high quality GaN single crystal was grown by MOVPE in 1985 [43]. The residual electron concentration of the GaN film grown with this method was reduced to a reasonable level of 10^{15} cm^{-3}. In 1991, the LT-buffer method was implemented by using LT-GaN buffer layer instead of LT-AlN buffer layer [44]. Nowadays, using of LT-GaN buffer layer is the standard choice in the growth of GaN and nitride alloys on sapphire by MOVPE.

Regardless of the dramatic improvement in the material quality, it was still not possible to produce p-type GaN. In 1992, high p-type concentration in GaN was achieved by thermal annealing of Mg-doped GaN [45]. It was found that it is essential to activate Mg acceptors by releasing hydrogen which passivates the Mg dopants. Conductivity control of n-type GaN was achieved by SiH_4 doping after decreasing the residual donors by using the LT buffer layer [3].

4.3 Epitaxial structure of III-nitride LEDs

A typical III-nitride LED structure, schematically shown in Fig. 4.2, consists of a GaN buffer layer, n-doped GaN layer, multi quantum well (MQW) stack, AlGaN electron blocking layer (EBL) and p-doped GaN layer grown on a substrate. A schematic band diagram of this structure is shown in Fig. 4.3. Years of material research over the world have been done for developing more advanced materials for these basic LED building blocks [1, 3, 4, 6, 18, 31, 34, 46]. The properties and the importance of each of the these layers for the LED performance will be discussed in the following text. Given that GaN is grown heteroepitaxially, the large lattice misfit between the substrate and the grown film leads to a high density of dislocations [47], which decreases the performance and lifetime of the LEDs [34]. Several approaches have been investigated for improving the material quality of the heteroepitaxially grown GaN [21, 48–51 and Publ. II].

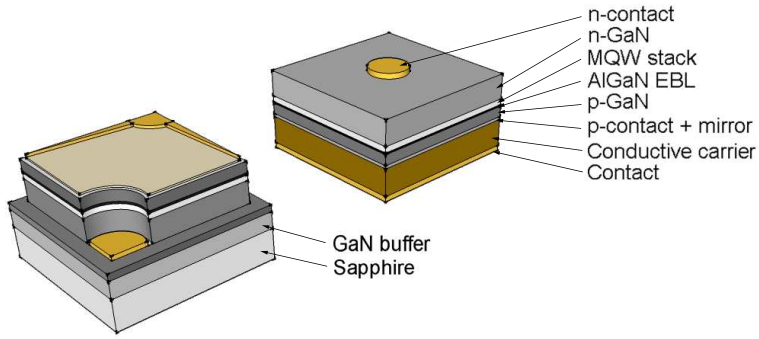

Figure 4.2. Different LED chip designs: a surface emitting chip (left) and a vertical chip (right). The light is extracted from the top side of the chips.

The typical n-type GaN layer of the LED is approximately 2 μm thick and doped with silicon impurity atoms for increasing the donor carrier concentration to the level of 10^{19} cm^{-3} [6]. GaN as a semiconductor has actually a n-type nature itself [18]. Generally the n-type doping of GaN is pretty straightforward compared to p-type doping. One just has to have high enough mobility and carrier concentration. However, it is essential to keep the electrical properties of n-type GaN in the certain optimal range for having a balance between n- and p-type layers. The balance is needed for locating the pn-junction into optimal position in the active MQW region [34].

The active region of the blue LED, where the actual light generation happens, usually consists of an InGaN/GaN MQW stack. The In content and width of the QWs determine the emission wavelength of the LED [52]. The MQW stack is under

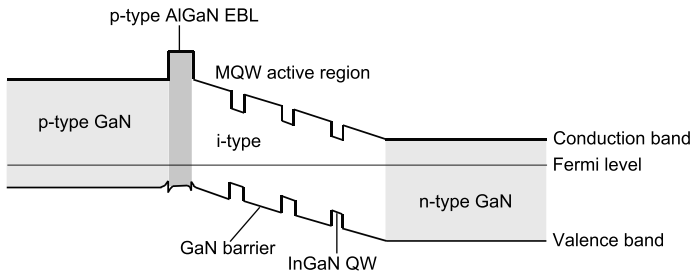

Figure 4.3. A schematic band diagram of the LED structure with doping. Fermi level is near the valence band in the p-type GaN and near the conduction band in the n-GaN. p-doping of the AlGaN EBL leads to band bending and higher effective barrier for electrons and lower effective barrier for holes. Both electrons and holes are trapped in the InGaN QWs having the smallest band gap in the structure.

considerable strain due to the large difference in the lattice and thermal constants of the InGaN quantum wells and GaN barriers. This strain generates a piezoelectric field inside the MQW stack [53]. Inside the QWs, the piezoelectric field-induced quantum-confined Stark effect (QCSE) results in red-shift of the QW emission energy and reduces the radiative recombination efficiency [52]. Growing a MQW stack is a challenging task due to the different optimum growth conditions of GaN and InGaN materials. GaN barriers also exhibit rough surface morphology which can deteriorate the quality of the MQW stack [Publ. IV]. Also fluctuations of the In composition inside and between the QWs influence the emission characteristics [54 and Publ. V].

The near-UV LEDs at the wavelength range of 370-400 nm still below the GaN absorption edge in photon energy limit, require thinner QWs and lower In composition compared to the blue LEDs in order to shift the emission peak to shorter wavelengths. The lower In content in the InGaN QWs decreases the potential well depth leading to reduction of the efficiency. The reduction of the potential well can be eliminated by adding Al into the barriers [55]. However, the different optimum growth conditions of the In and Al containing GaN alloys makes it challenging to obtain good quality InGaN wells and AlGaN barriers with desired composition in the same MQW stack. For improving the quality of low temperature AlGaN a small amount of In can be introduced into the barrier layers [Publ. VI and Publ. VII]. More detailed discussion about growth and properties of the active layer is described in sections 5.3. and 5.4.

A wide band gap EBL is often utilized between the active layer and the p-type contact layer of the structure [34]. In GaN-based blue and UV LED structures

Mg-doped p-type AlGaN EBL is commonly employed to prevent electron overflow from the active region to the p-type contact region [56]. The growth parameters and placement of the AlGaN EBL can significantly affect the efficiency and operating characteristics of the structure [Publ. VIII]. The wide band gap leads to conduction and valence band offsets, which means that that EBL blocks holes as well as electrons. The hole blocking can be avoided with Mg-doping which leads to band bending and higher effective barrier for electrons and lower effective barrier for holes. The MOVPE growth of high quality AlGaN EBL is a challenging task. Typically Mg-doped AlGaN has a lower structural and electrical quality than p-type GaN. For this reason the thickness of the EBL should be optimized carefully [Publ. VIII]. The doping level also has a significant impact. Too low level increases the serial resistance of the structure and too high level tends to decrease the crystal quality which leads to degradation of the electrical properties [56–58 and Publ. VIII]. Growth and properties of the AlGaN EBL layer will be discussed in more detail in section 5.5.

Growth of p-type GaN with reasonable quality and doping level was the main bottleneck in the III-N technology for a long time [3, 6]. Typically Mg acceptors are passivated by H_2 during the MOVPE growth of p-type GaN [45]. For achieving the p-type conductivity the Mg acceptors in MOVPE grown p-type GaN need to be activated. This is usually done either by in situ annealing in the MOVPE reactor or by post growth annealing [57]. However, after activation p-type GaN typically still has one decade lower carrier concentration and mobility compared to n-type material. For this reason the pn-junction is located near the p-GaN interface. This decreases the performance of the LED structure [34] and it is one reason for using the AlGaN EBL in the structure [56]. Another challenge related to the p-type GaN has been the fabrication of low resistance ohmic contacts. Low contact resistance is difficult to obtain because of the difficulty to achieve high hole concentrations in p-type GaN and the lack of metals with high work function compared to the band gap and the electron affinity of GaN [59].

4.4 Light extraction from LEDs

One challenge in the LED design has always been to achieve efficient light extraction from the structure. Even though the light is efficiently generated in the active region, it cannot escape from the semiconductor heterostructure if it is totally reflected at the semiconductor-air interface [34]. Also absorbtion caused by the p- and n-contacts decrease the light extraction efficiency [60]. During the years many different approaches like highly transparent conductive oxide contact materials [60–63], flip-chip device structures [1, 64] and sophisticated vertical chip technologies [65–67] have proven to be successful to enhance the light intensity radiated from a III-N based semiconductor LED. A schematic of these LED chip designs is shown in Fig. 4.2. Typically these methods are combined with roughening and/or patterning of the material surface [68–70], and using highly reflective mirror layers [71].

In principle, objects scatter light efficiently when the ratio of the wavelength inside the material to the object dimension is between 1/10 and 2. The scattering efficiency has a maximum when the ratio is between 1/3 and 1 [72]. This is the main reason why the surface of the LED or substrate material is often tailored in order to improve light extraction. A little bit more sophisticated method is to use a photonic crystal structure in order to guide the light out [73]. However, the short wavelength of the nitride based LEDs makes it difficult to achieve dimensions needed in these methods with traditional photoresist technologies. Hence, either a nanoimprint [73] or a maskless [69 and Publ. I] approach is typically applied. The advantage of the maskless strategy compared to nanoimprint structures is that scattering objects are randomly created. Consequently, preferred directions with glancing angles and the disadvantage of the periodic pattern of similar structures will be avoided. In addition these maskless processes are often time saving and cost effective.

Another interesting approach for increasing light extraction is utilization of a patterned substrate which efficiently scatters the light emitted from the active layer. Theoretically light extraction can be increased significantly compared to the unpatterned LED when an optimal substrate patterning is used [74]. However, the nature of the available substrate materials and useful patterning methods limit the options to variate patterns on the substrate. Especially, the chemically inert nature of sapphire makes patterning a challenging task. However, a number of different patterns fabricated with several methods have been successfully used to enhance light extraction from III-N LEDs [51, 75–78 and Publ. III]. Patterning of sapphire substrates and MOVPE growth on them will be discussed in more detail in sections 5.1 and 5.2.

An interesting future approach regarding the LEE of LEDs is employing some method of coupling the energy to surface-plasmons. The amount of energy coupled into these modes could allow still greater enhancement of the LED efficiency than existing methods [79, 80]. This phenomenon has recently received a great deal of interest in the scientific community.

5 Approaches for optimizing the III-N LED structure

In this chapter the MOVPE growth and properties of several III-N based heterostructures, mentioned as building blocks previously in the previous chapter 4, are discussed. The influence of these building blocks on the optical and electrical properties of LED structure are described.

5.1 Patterning of sapphire substrate

Mechanically and chemically strong nature of sapphire makes patterning a challenging task. Sapphire is known to interact with some melted salts, alkalis, acids, extremely hot H_2 vapor at over 1300 ^{o}C and plasma etchants [29, 76, 81]. However, in practice three methods are used for patterning epitaxial grade sapphire: inductive coupled plasma reactive ion etching (ICP-RIE) [76, 81], high temperature wet etching [78, 82, 83] and laser-assisted wet etching [84]. The main difference between these methods is the anisotropic and crystal plane depended natures of ICP-RIE and wet etching, respectively. For this reason wet etched patterns on sapphire have mainly been holes on the surface [85]. With plasma methods a wider range of patterns have been fabricated [50, 51, 75, 76, 85, 86].

In this work the sapphire patterning and/or roughening was done by using H_2SO_4:H_3PO_4 acid mixtures with different ratios in the temperature range of 240-320 ^{o}C. SiO_2 and SiN were tested as etching mask material. SiN was shown to be a poor mask choice with very low selectivity compared to c-plane Al_2O_3. SiO_2 tolerated the etching mixture well and offered selectivity between 35-115 depending on the etching temperature and chemistry. Fig. 5.1 depicts the etch rate of c-plane sapphire as a function of temperature in the H_2SO_4:H_3PO_4 3:1 mixture. The results obtained show a five fold increase in the etching rate as the etching temperature is increased from 280 ^{o}C to 320 ^{o}C. According to literature etch rates of over 1 μm/min have been achieved for c-plane sapphire [83, 87]. Etching solution offered an excellent uniformity with less than 0.5 % difference over the sample which can be seen also in Fig. 5.1 a). SEM image of the etched Al_2O_3 surface is presented in Fig. 5.2 a) indicating the crystal plane depended nature of etching, which has been

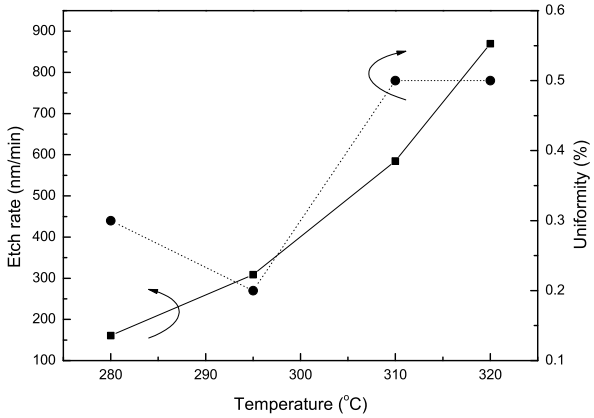

Figure 5.1. Temperature dependence and uniformity of the Al_2O_3 c-plane etch rate in 3:1 H_2SO_4:H_3PO_4 solution.

studied in more detail elsewhere [29, 83]. Etch rates for different sapphire crystal orientations as reported in the literature are shown in Table 5.1.

Table 5.1. Al atomic packing density and etch rates of sapphire orientations using 3:1 H_2SO_4:H_3PO_4. Modified from Kim et al. 83.

Crystal plane	Orientation of sapphire ($hkil$)	Al atomic surface density (cm^{-2})	Etch rate (nm/min)			
			282 °C	300 °C	312 °C	321 °C
c-plane	(0001)	$10.18 \cdot 10^{14}$	188	418	790	1148
a-plane	$(11\bar{2}0)$	$5.59 \cdot 10^{14}$	15	45	58	105
r-plane	$(\bar{1}012)$	$4.09 \cdot 10^{14}$	67	227	553	813
m-plane	$(10\bar{1}0)$	$3.23 \cdot 10^{14}$	23	80	177	240

It was noticed that pure H_2SO_4 etching had poor uniformity, unstable etch rate and poor selectivity between Al_2O_3 and the SiO_2 etch mask (Fig. 5.2 b) and c)). The quality of etching was found to improve significantly when a small amount of H_3PO_4 acid was added into the H_2SO_4 solution. It was found that an etching mixture (H_2SO_4:H_3PO_4) ratio as high as 100:1 was able to improve the uniformity by up to 10 times. Figs. 5.2 b) and c) show that when pure H_2SO_4 was used pyramid structures were created due to the increased selectivity between the crystal planes and redeposition of the insoluble reaction products of etched material. A remarkable role of the redeposition can be seen from Fig. 5.2 b) where the redeposited material appears also on top of the SiO_2 etching mask. On the other hand, a comparison of

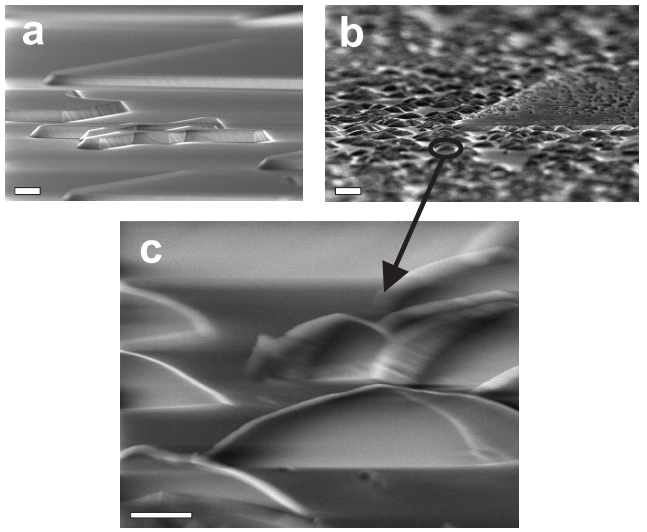

Figure 5.2. SEM images from the c-plane epi-ready sapphire surface after wet etching. It can be clearly seen from the image a) that the etching mixture of H_2SO_4 and H_3PO_4 offers a smooth etched surface. Images b) and c) show that in the case of pure H_2SO_4 etchant there is material redeposition and a strong crystal plane dependence of the etching. Image b) also shows redeposition of the material on the SiO_2 mask. The scale bars correspond to 10 μm in a) and b) and to 2 μm in c) [Publ. I].

the size of the redeposited objects and the created pyramid structures indicates that the redeposition rate was lower than the etching rate. So a probable reason for the creation of the pyramids, which is seen in Fig. 5.2 c), is self masking caused by the redeposited insoluble reaction products of etched material followed by the crystal plane depended etching.

The non polished back side of the c-plane sapphire substrate has typically an average roughness of 0.7-1.2 μm depending on the supplier. A set of non patterned sapphire samples were treated in pure H_2SO_4 at 300 ^{o}C for 5, 15 and 60 min. Fig. 5.3 a) shows a SEM image of the non etched back side surface of the sample. When the back side was treated with pure H_2SO_4 scattering objects were created on the surface as shown in Figs. 5.3 b), c) and d). It can be seen that the average size of the created objects can be controlled easily by varying the etching time.

The possibility to tune the size of the scattering objects with pure H_2SO_4 in order to enhance light extraction from the backside of the sapphire wafers was investigated in Publ. I. Fig. 5.4 shows the EL output power versus driving current from the similar LED structures on the conventional sapphire (CS) and on the H_2SO_4 back

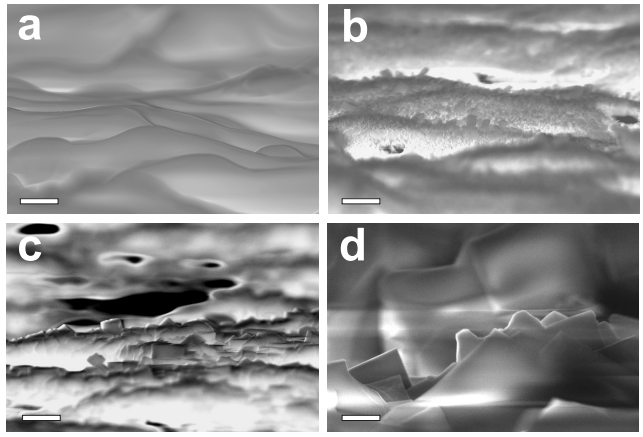

Figure 5.3. SEM images of the non polished sapphire backsides after H_2SO_4 roughening for a) 0 min, b) 5 min, c) 15 min and d) 60 min. It can be seen that the size of the scattering sapphire objects can be controlled with the etching time. The scale bars correspond to 1 μm [Publ. I].

side roughened sapphire. LED on the roughened substrate offered a 20-25 % higher EL output power in the backside measurement compared to the reference LED without exceptions in the whole current range. This is a strong evidence that the pure H_2SO_4 treatment offers a maskless surface roughening method to increase light extraction in LED applications such as flip chip LEDs in which light is extracted from the backside of the sapphire substrate.

5.2 Growth of GaN on conventional and patterned sapphires

Growth of GaN on sapphire has been known to produce grains on the sub-micron scale with grain boundaries having TDs [47]. Several approaches such as epitaxial lateral overgrowth (ELOG) [48], pendeo epitaxy (PE) [49], multistep method (MSM) [21], patterned sapphire substrates (PSSs) [50], and combinations of these methods [51] have been successfully proposed for reducing the TD density. A drawback of the ELOG and PE methods is that one needs to perform epitaxial growth twice. MSM and PSS have an advantage of a single epitaxial growth. Improved GaN material quality has been reported when the epitaxial structure has been grown on a PSS [51, 75, 78, 85, 88].

In this work GaN growth on PSSs having a direct and an inverse pattern was investigated. The first pattern called as direct pattern contained etched hexagonal holes on the sapphire (HS) having a diameter of 2.5 μm and a spacing of 2.5 μm

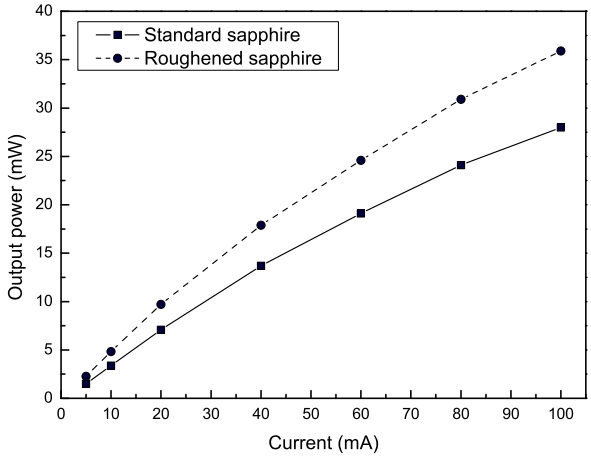

Figure 5.4. EL output power as a function of injection current. The plot clearly shows the increased EL output of the LED on the roughened sapphire [Publ. I].

shown in Fig. 5.5 a). The second pattern was an inverted version of the first pattern having pillars on the sapphire (PS), shown in Fig. 5.5 b). Depth and height of these structures can be seen in Figs. 5.6 a) and b). The GaN films were grown on HS, PS and reference CS substrates in the same epitaxial run by using the standard two step growth method. A low-temperature nucleation layer was followed by a 2.5 μm thick undoped GaN layer grown at the pressure of 200 Torr at the standard GaN growth temperature of 1050 ^{o}C. A TMGa molar flow rate of 185 μmol/min and an ammonia flow of 3500 sccm were used during the growth of the thick GaN layer.

Figs. 5.5 c) and d) show the SEM images from the GaN films after growth interruption from HS and PS substrates, respectively. On the HS substrate (Fig. 5.5 c)) growth initiates only on the c-plane, but not on the etched planes. When growth is continued a free standing GaN grows laterally over the etched hole. On the PS substrate (Fig. 5.5 d)) GaN grows also on the c-planes. However, in this case GaN grows on two different levels: on the top and between the hexagonal sapphire mesas. During the growth the ground level is filled by coalescence of the nucleation islands leading to vertical GaN growth. On the other hand GaN islands originating from the higher level continue lateral growth overlaying the ground level GaN film.

It has been previously reported that vertical growth of freestanding GaN cantilevers produces very few TDs on the free standing area [50]. Figs. 5.7 a), b) and c) show

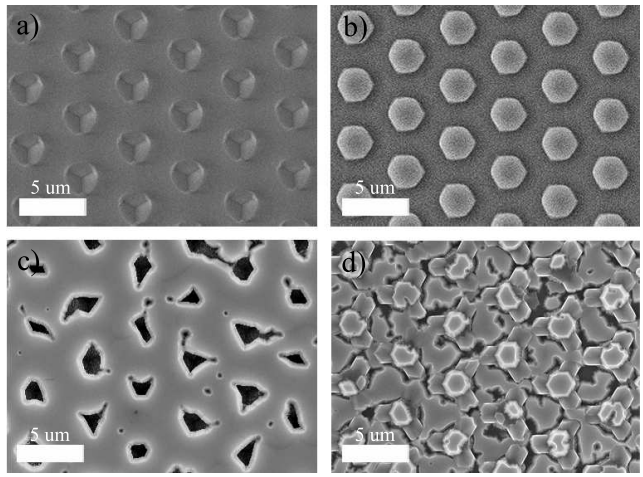

Figure 5.5. SEM images from a) the HS substrate, b) the PS substrate and c) GaN film after growth interruption on the HS substrate. Free standing GaN seems to grow horizontally over the holes. d) SEM image from the GaN film after growth interruption on the PS substrate. It can be seen that the GaN film grows on two different levels: on top of the pillars and on the bottom of the PS substrate [Publ. II].

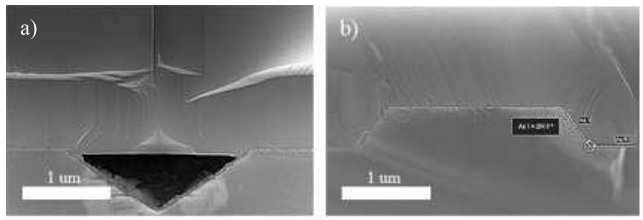

Figure 5.6. Cross section SEM images of the GaN films grown on a) the HS substrate and b) the PS substrate. The free standing GaN covers the holes on the HS substrate leaving air holes between the sapphire and GaN interface. On the PS substrate GaN covers the substrate completely. [Publ. II].

the AFM etch pit density (EPD) scans from the GaN surface grown on the CS, HS and PS substrates, respectively. It can be noted that there are clear differences in the dislocation densities although the density level is in the scale of 10^8-10^9 cm^{-2} for all the samples. It can be noted from Fig. 5.7 c) that there are concentration points (CPs) of dislocations (circulated areas). It was found from various AFM scans that these CPs follow the periodicity of the pillars on the PS substrate and that the points are located on top of the pillars. In contrast the areas around the CPs

contain very few dislocations. The reduction of the dislocation density around the CPs is possibly caused by dislocation bending [89, 90] on the inclined facets during GaN growth since the substrate surface is still separated into many grains instead of full coalescence on the PS substrate. Surface adatom diffusion is interrupted at the boundaries of the grains, leading to separate growth within each grain. The lateral facets of GaN in each grain become inclined. When propagating vertically near such inclined facets TDs bend at 90^o paralleling the (0001) facet. As a result, the crystal quality of GaN around the CPs is improved. The sample grown on HS substrate showed clearly the lowest dislocation density (Fig. 5.7 b)). However, similar periodicity as in the PS case was not found.

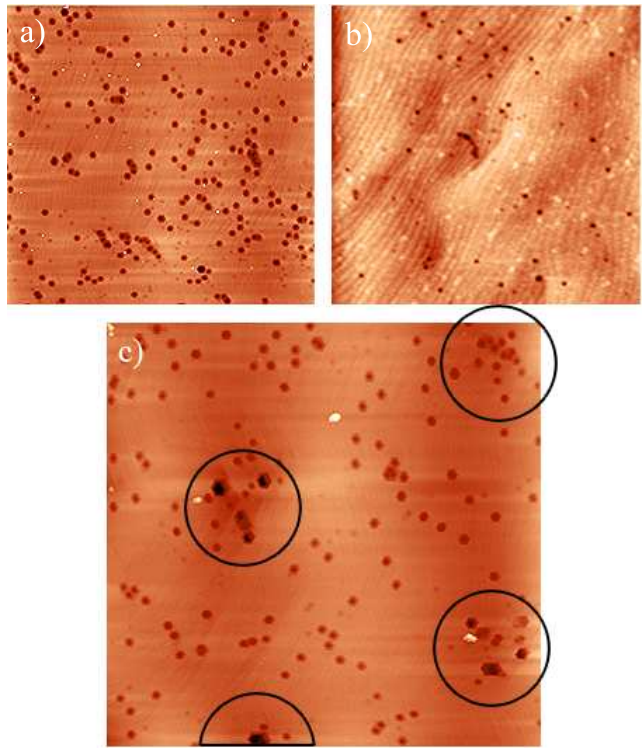

Figure 5.7. 10x10 μm^2 AFM EPD scans from a) the reference sample, b) the GaN film on HS substrate, and c) the GaN film on PS substrate. It can be noted that the reference sample has the highest TD density. In the PS substrate case there are concentration points of the TDs. These circulated points follow the periodicity of the pillars on the PS substrate [Publ. II].

Fig. 5.8 presents XRD scans of the GaN (002)-reflection from the samples. Also the calculated theoretical strain free lattice constant angle is shown. The lattice constant (LC), full width at half maximum (FWHM) of the XRD peak and strain

parameters were calculated from the measurements and are shown in Table 5.2. For the operation of GaN-based devices strain in the a-direction has a more significant role compared to strain in the c-direction because the GaN film grows along the [001] vector. It can be noted from Table 5.2 that LCs for all the samples are smaller compared to the theoretical value refering to compressive strain. The sample grown on the PS substrate has the a-direction LC nearest to the theoretical value and also the highest difference compared to the reference CS sample. The LC in a-direction in the sample grown on the HS substrate is practically equal compared to the CS sample. It can be verified that the PS sample has relieved strain compared to the GaN film on the homogenous c-plane sapphire substrate. However, it should be noted from Fig. 5.8 that there are two peaks in the XRD curve from the PS sample indicating that the sample contains GaN with two different LCs: one with relived strain and the other with LC nearly similar to the standard GaN grown on the CS substrate. It can be also noted from the FWHM values in Table 5.2 that there is a slight decrease and increase in the FWHM for the HS and PS samples, respectively, compared to the reference CS sample. The decrease of the (002)-reflection FWHM has been attributed to the decreased density of dislocations with a screw component [21].

Table 5.2. XRD-results from the (002)- and (112)-reflections [Publ. II]

Sample	CS	HS	PS
$2\theta_{002}$	34.53943	34.54078	34.55149
$2\theta_{112}$	69.19301	69.19335	69.18374
a [Å] ±0.0017	3.1829	3.1830	3.1839
c [Å] ±0.0014	5.1893	5.1891	5.1876
ε_a [%] ±0.0528	-0.1893	-0.1884	-0.1604
ε_c [%] ±0.0266	0.0837	0.0799	0.0498
ε_{aA-1} [%]	0	8.33719E-6	2.88904E-4
ε_{cA-1} [%]	0	-3.78934E-5	-3.38408E-4
FWHM_{002}	0.0090	0.0085	0.0125
FWHM_{112}	0.0447	0.0404	0.0704

Next, two sample series were fabricated in order to investigate how the pattern depth and density affect the GaN film quality and LED light extraction. Two different masks were used for patterning. A low density pillar structure (LDPS) and a high density pillar structure (honeycomb) consisting of hexagonal pillars having 4 μm diameter with 3 μm spacing and 3 μm diameter with 1.5 μm spacing, respectively. Three different pillar depths of 300, 550 and 700 nm for LDPS and three depths of 500, 800 and 1300 nm for honeycomb pillars were fabricated. GaN growth consisted of a low-temperature nucleation layer and a 2.5 μm thick undoped GaN buffer grown at elevated temperature followed by a 2μm thick undoped GaN grown at standard GaN growth temperature. The growth was performed in H_2 atmosphere. In the LED samples the buffer GaN films for conventional and patterned sapphires were grown

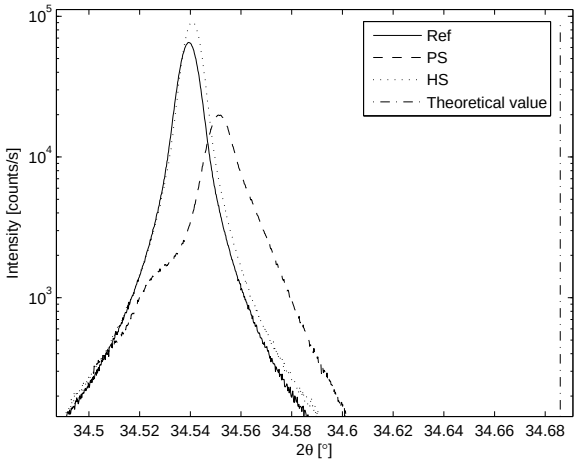

Figure 5.8. XRD rocking curve of (002)-reflection from the GaN films on different substrates. With PS sample there are two peaks indicating that the sample contains GaN with two different LCs with relived strain and with the nearly similar strain compared to GaN grown on the CS and HS substrates [Publ. II].

with the same growth process as described above. The LED structure emitting at 405 nm was grown with a procedure described in more detail in section 5.5.

The samples had a smooth surface morphology which can be observed from AFM scans in Figs. 5.9. a) and b). For investigating the influence of the pattern type on the TD density AFM EPD scans were taken from the samples. Fig. 5.9. c) and d) show the difference between the EPDs in the cases of CS and honeycomb sapphire, respectively. There is a five fold difference between the TD density levels of $1.04{\cdot}10^9$ cm^{-2} and $2.1{\cdot}10^8$ cm^{-2} between these samples. The behavior of the EPD as a function of pillar depth is shown in Fig. 5.10 for GaN films on both LDPSs and honeycomb PSSs. The plot clearly shows that with honeycomb pattern the pillar depth does not have a huge influence on the TD density. However, the TD density with all the depths is much lower compared to the case of CS substrate. In the case of LDPS the pillar depth is much more crucial. It can be observed that even as low pillar depth as 300 nm decreases the TD density level to the same level as on the honeycomb sapphires but then the TD density increases rapidly with the increase of the pillar depth. The improvement in the crystalline quality of the GaN films using LDPS, honeycomb PSSs and CSs are shown in Table 5.3, where the EPD and XRD data are summarized.

The optical properties of the LED samples are summarized in Table 5.4. It can be noted that all the LED samples grown on honeycomb sapphires showed an enhanced PL intensity compared to the reference sample grown on CS. However, it can be

Table 5.3. Summary of EPD and XRD measurements from the GaN films grown on LDPS, honeycomb and reference CS substrates with various pillar depths [Publ. III].

Substrate			XRD-FWHM	
Mask	Depth	EPD	002	302
	(nm)	(cm^{-2})	(arc sec)	
CS	-	$1.04{\cdot}10^{9}$	12	192
LDPS	300	$3.5{\cdot}10^{8}$	12	189
LDPS	550	$3.8{\cdot}10^{8}$	14	184
LDPS	700	$6.6{\cdot}10^{8}$	15	172
Honeycomb	500	$2.2{\cdot}10^{8}$	13	198
Honeycomb	1050	$2.1{\cdot}10^{8}$	13	145
Honeycomb	1300	$2.6{\cdot}10^{8}$	14	181

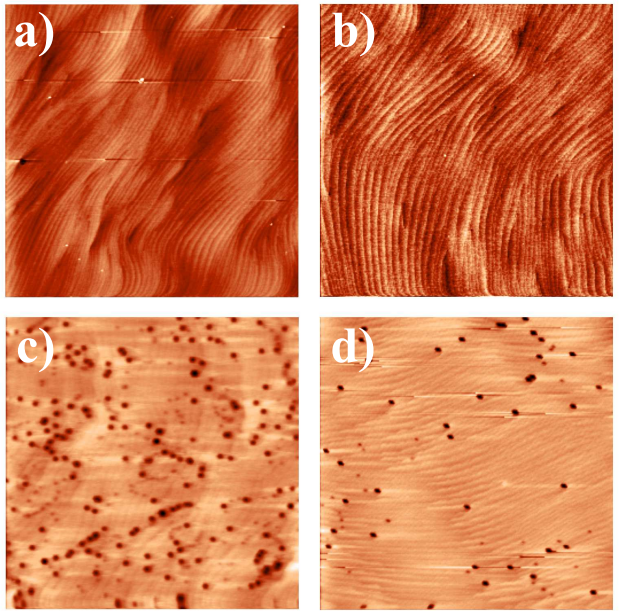

Figure 5.9. 5x5 μm^2 AFM surface scans of a) a reference GaN template sample grown on CS and b) a GaN template grown on honeycomb sapphire with a pillar depth of 1050 nm. From both GaN surface scans a smooth surface with clean atomic steps can be observed. AFM EPD scans from the GaN layers grown c) on CS and d) on honeycomb sapphire with pillar depth of 1050 nm [Publ. III].

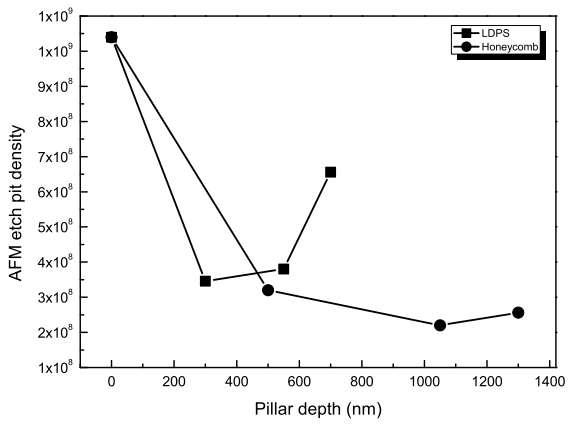

Figure 5.10. AFM EPD of the samples grown on both pattern types (LDPS and honeycomb) with different pillar depths. Plot shows that PSSs offer lower density of dislocations with all pillar depths. However, the optimum depth depends on the pattern. With LDPS lower pattern depths are optimal. [Publ. III].

noted from Table 5.4. that with LDPS LEDs only the sample grown on the substrate with the highest pillar depth of 700 nm shows significantly higher PL intensity compared to the CS LED. A correlation between the increased PL intensity and the reduction of the TD density was not observed. A more obvious correlation can be seen between the increased PL intensity and the increased pillar depth with LEDs grown on LDPS sapphires. Obviously, when the pillar depth increases the relative area of the exceptional crystal planes compared to the area of the c-plane increases. Thus, increasing LEE is achieved with the increasing pillar depth. In the case of the honeycomb pattern one idea in the original design was to have higher area ratio between the exceptional planes and the c-plane. For this reason the LEE of the LEDs grown on honeycomb sapphires is already high with pillar depth of 550 nm and it is not increasing with increasing pillar depth. These results indicate that the improvement of the PL intensity is mainly caused by the enhanced LEE. The increase in the PL efficiency in most of the samples was fairly high. In other studies it has been simulated and measured that ICP etched stripe patterns on the sapphire substrate cause an increase of over 20 % in the LEE [85]. In the case of chemically wet etched PSSs the increase of the LEE can be even higher because the sidewalls of the patterns are inclined unlike the almost vertical sidewalls of the ICP etched sapphire substrate [88].

For further clarification of the issue between IQE and LEE a temperature dependence of the integrated PL intensity of the honeycomb and reference samples

Table 5.4. Optical performance of the InGaN/GaN LEDs grown on LDPS, and honeycomb substrates with different pillar heights and CS substrate. The PL, top side EL, and bottom side EL intensity values of reference sample are scaled to 100. EL intensity values are averaged from the best 10% of the operating chips measured around each wafer. Modified from [Publ. III].

	Substrate		RT PL			RT/LT PL	EL int. at 20 mA		
Sample	Mask	Depth	Int.	λ	FWHM	ratio	Top	Bottom	λ
		(nm)	(a.u.)	(nm)	(nm)	(a.u.)	(a.u.)	(a.u.)	(nm)
REF-LED	CS	-	100	400	15	100	100	100	404
L-LED1	LDPS	300	98	409	15	-	116	110	410
L-LED2	LDPS	550	117	400	15	-	95	87	405
L-LED3	LDPS	700	162	406	16	-	93	81	408
H-LED1	Honeycomb	500	167	400	13	109	132	119	406
H-LED2	Honeycomb	1050	165	400	13	94	121	111	405
H-LED3	Honeycomb	1300	158	404	14	93	130	119	409

was measured. The ratios between the PL intensities of the LT and RT measurements are also summarized in Table 5.4. It can be noted that only the sample H-LED1 has an improved IQE while the other two honeycomb samples have actually a little bit lower IQE compared to the reference sample. However, all the IQEs are in the same range and big differences between patterned and non patterned samples did not exist as in some studies [61, 77, 78].

From the EL results, shown in Table 5.4, it can be noted that the sample L-LED1 grown on the 300 nm deep LDPS sapphire which had a similar PL efficiency as the reference LED has higher EL output than the reference LED. However, in case of the other LEDs grown on PSSs the increase of EL intensity is lower than the increase of the PL efficiency. Samples L-LED2 and L-LED3 with an improved PL efficiency were showing actually a little bit lower EL output compared to the reference sample. However, TD densities in samples L-LED2 and L-LED3 were lower than in the reference sample. So the TD density is not explaining lower EL intensity. SEM surface scans were taken from these two samples in order to investigate the unexpectedly low EL intensity. It was observed from these scans that the p-GaN surface in these samples contains small scale holes. These holes are probably originated from the more challenging coalescence process during growth on the LDPS sapphire. Some of these holes can act as micro channels for carriers over the active region lowering the efficiency of the operating device. This gives an explanation why the PL intensities of these samples were so high considering that PL is giving the information on the material properties of the active region while EL is also influenced by the transport properties of the structure.

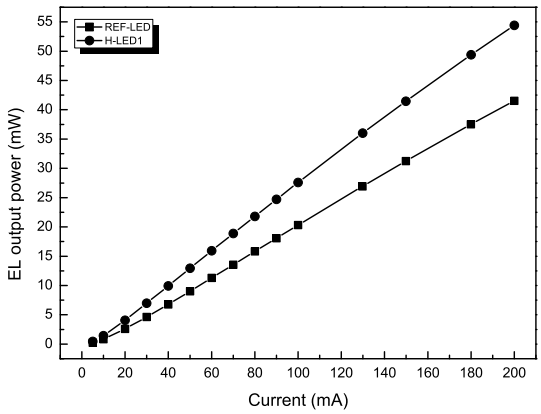

Figure 5.11. EL output power as the function of driving current from the best individual chips of the samples H-LED1 grown on the honeycomb substrate and REF-LED grown on the CS. H-LED1 shows a higher EL output over the whole current range from 5 mA to 200 mA. [Publ. III].

It is believed that TDs may act as diffusion pathways for Mg generating a carrier path over the active region of the LED and, therefore, may influence the EL emission efficiency [51]. It has also been stated that the decreased TD density caused by the use of PSSs increases the EL efficiency [51, 85, 86]. Also it is supposed that in UV-LEDs the TDs might decrease the light output more due to the limited self screening mechanism in InGaN/GaN quantum wells caused by smaller In composition [91, 92]. However, according to our results the enhanced LEE has a major role and the choice of the optimal patterning for light extraction is the most important factor with PSSs while the TD reduction effect from the level of 10^9 cm^{-2} to the level of $2{\cdot}10^8$ cm^{-2} has only a minor role.

Fig. 5.11. represents the measurement results of the RT EL intensity as a function of driving current. The data was obtained from the best individual chips of the LEDs grown on the CS and honeycomb sapphire. There was no significant current depended efficiency variation between the samples. Fig. 5.12. shows the current-voltage (I-V) curves of the samples on the CS and honeycomb sapphire. Very low level forward voltages 3.24 V and 3.37 V were measured at 20 mA driving current, respectively. The forward voltages in the LEDs grown on PSS were always a little bit higher than in the reference LED grown on the CS as shown in Fig. 5.12. The reason for this behavior was found to be related to the n-type material. Resistance values between n-type contacts of the chips next to each other were higher in the LEDs grown on the PSSs than on the CS. This indicates that the total volume

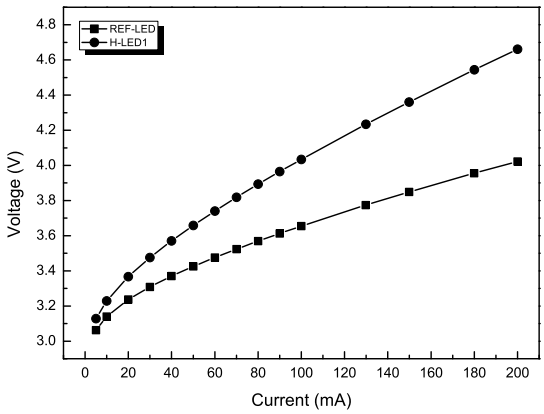

Figure 5.12. I-V curves of the LEDs H-LED1 grown on the honeycomb substrate and REF-LED grown on CS. As can be seen from the plot, sample H-LED1 had a little bit higher voltage values compared to the reference LED. Similar behavior was observed with all the LEDs grown on PSSs [Publ. III].

of the low resistance n-type GaN is somehow decreased when the LED structure is grown on the PSS. In previous studies the forward voltages with PSSs have been reported to be lower, similar and higher compared to CSs [51, 78, 85]. According to our results the different n-type GaN thickness might have been one reason for the contradictory behavior in the other studies.

5.3 InGaN/GaN quantum wells for blue LEDs

Indium compositions higher than 15 % are required in the InGaN QW layers [6] for blue LEDs. However, the parameter window for growth of good quality InGaN with such a high In content is small. Typically growth temperature below 800 ^{o}C and optimized growth rate to avoid desorption of In are needed [93]. It is also known that the presence of hydrogen ambient significantly reduces the In incorporation efficiency. Therefore, nitrogen environment is used during the growth of InGaN layers. InGaN layers grown outside the optimum parameter window have deteriorated crystal quality and poor optical performance. The major challenge in the growth of a high performance InGaN/GaN MQW stack is that the optimum growth parameters for high quality GaN including hydrogen ambient and temperature in excess of 1000 ^{o}C are far from the InGaN growth regime. Thus, some compromises and tricks are required while growing the active region.

Surface of a GaN barrier on top of an InGaN QW layer is characterized by the presence of pits with inclusions located in the center of the pits when constant temperature and nitrogen atmosphere are used in the growth of MQW stack [94, 95 and Publ. IV]. These pits, named as V-defects, are generated at the ends of TDs [96–101] due to strain induced mechanisms and/or the different growth rates of separate crystal orientations during InGaN layer growth. It has been proposed that the low temperature growth of GaN, on top of InGaN layer, causes three dimensional nucleation of GaN at the In rich cluster hiding at the apex of the V-pit [102]. During the barrier growth, the inclusions propagate through the barrier layer resulting in unsharp interfaces between the QWs and the barriers and in non-planar surface of the MQW stack. This progressively deteriorates the morphology of the successive QWs. However, due to the potential landscape of the V-defect the sidewall seems to screen the defects themselves, which protects the device performance and reliability [91].

The other issue is that the MQW stack is under considerable strain due to the large difference in the lattice and thermal constants of the InGaN QWs and GaN barriers. A piezoelectric field inside the MQW stack is generated by this strain [53]. The strain can also cause a complete relaxation of the structure with high enough In content. Inside the QWs the piezoelectric field-induced QCSE results in red-shift of the QW emission and reduces the radiative recombination efficiency [52]. Also fluctuations of the In composition influence the emission efficiency in the QWs [54].

In this work we compared several methods including increased barrier growth temperature [103], growth interruption (GI) after the InGaN layer growth [104, 105] and a barrier hydrogen treatment [102, 105] in order to improve the surface morphology of the InGaN/GaN quantum well structures. Samples contained 5 InGaN/GaN QWs grown on top of the GaN buffer. During the growth of the MQW stack the pressure was 300 Torr. TMI/(TMI+TMGa) ratio of 0.7 and temperature of 745 ^{o}C and N2 ambient were used during the InGaN layer growth. The In composition was targeted at 15 % and the QW and barrier thicknesses were fixed at 3 nm and 10 nm, respectively. The reference sample A was grown using constant temperature and nitrogen atmosphere during the growth of MQW stack. The effect of increased barrier growth temperature was tested in a sample series, where the InGaN QWs were first protected by a 2 nm thick GaN layer grown in the same conditions as the QWs. Then the temperature was increased to 900-960 ^{o}C for the remaining 8 nm of the barrier growth. The influence of GI was tested by stopping the barrier growth for 5-50 s after the deposition of each 2 nm protective GaN layer and before the deposition of the 8 nm thick GaN barrier at 900 ^{o}C. The hydrogen treatment was investigated with samples having GaN barriers grown at 900 ^{o}C and the H_2/N_2 carrier gas flow ratio during the barrier growth. H_2/N_2 ratio was varied between 0.02 and 0.2.

AFM scans of the surface morphology of the samples are shown in Fig. 5.13. It can be noticed by comparing Figs. 5.13 a) and b) that elevated barrier growth

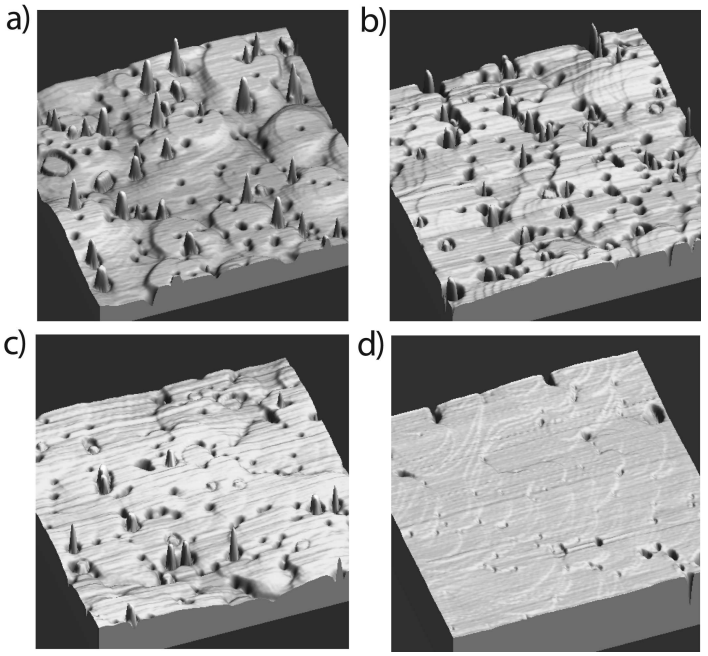

Figure 5.13. 3 x 3 μm^2 AFM surface scans of the MQW samples grown with following parameters: a) carrier gas during barrier growth: N_2, $T_{barrier}$ = 745 ^{o}C, b) carrier gas during barrier growth: N_2, T_{well} = 745 ^{o}C, $T_{barrier}$ = 900 ^{o}C, c) carrier gas during barrier growth: N_2, T_{well} = 745 ^{o}C, $T_{barrier}$ = 900 ^{o}C, growth interruption 20 s and d) carrier gas during barrier growth: H_2/N_2 = 0.02, T_{well} = 745 ^{o}C, $T_{barrier}$ = 900 ^{o}C. The height scale in all the figures is 20 nm [Publ. IV].

temperature of 900 ^{o}C does not eliminate the pits nor the inclusions. However, a smoother surface outside the pits can be observed. It can be noted from PL results in Fig. 5.14 that the reference sample A has luminescence peak from the InGaN QWs at 480 nm and a long-wavelength shoulder at 500 nm, which is probably caused by the fluctuations of the In content. The same kind of shoulder cannot be observed from the sample grown with elevated barrier temperature. Further increase of the barrier growth temperature up to 960 ^{o}C results in much smoother surface morphology. However, optical quality of InGaN QWs is severely reduced. Increasing the GI time from 5 to 20 s caused a gradual reduction of the inclusions. The surface of the sample with a 20 s GI is shown in Fig. 5.13 c). The number of inclusions, and consequently, the number of In rich clusters is slightly reduced compared to the reference sample A (Fig. 5.13 a)), and the layer morphology is improved. However, the PL spectrum did not change at all. Increasing the GI time to 50 s caused degradation of the PL intensity with no visible change in surface

morphology.

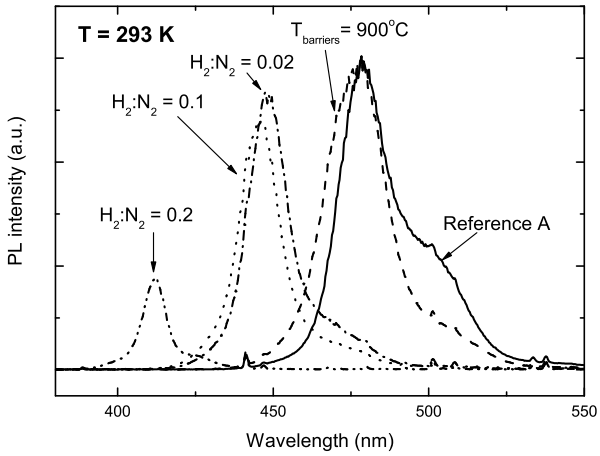

Figure 5.14. RT PL spectra of the samples with different growth procedures of the GaN barriers in an InGaN/GaN MQW structure: solid line - reference sample A, dashed line - GaN barriers grown at 900 ^{o}C, dash-dot line - H_2/N_2 ratio 0.02, dot line - H_2/N_2 ratio 0.1 and dash-dot-dot line - H_2/N_2 ratio 0.2 [Publ. IV].

The effect of hydrogen on the MQW structure was studied by variating the flow ratio of H_2 and N_2 between 0.02 and 0.2. Even as small H_2/N_2 ratio as 0.02 completely eliminates the inclusions resulting in a smooth GaN surface (Fig. 5.13 d)). H_2 removes the In rich clusters via enhanced In desorption which can be seen as an improved planar morphology. Hydrogen in the carrier gas mixture lead also to a 30 nm blue shift of the PL peak position. Simultaneously, narrowing of the main PL peak down to FWHM of 16 nm was observed. The blue shift and the narrowing of the FWHM are related to the reduction of the average In content and to the increased compositional uniformity in the quantum wells. In the XRD diffraction scan (Fig. 5.15) the sample grown with the H_2:N_2 ratio of 0.02 has stronger and more pronounced higher order satellite peaks compared to the reference sample indicating improved structural quality of the MQW structure.

Inserting an $In_xGa_{1-x}N$ layer under the MQW stack is known to improve the emission efficiency of MQWs [106–108]. In this work we performed a study on the role of the $In_xGa_{1-x}N$ underneath layer (UL) with In contents in the range of 0-2.7 % on the performance of InGaN/GaN LEDs operating in the spectral range from 425 nm to 460 nm. The LED samples contained a 2μm thick n-type GaN layer

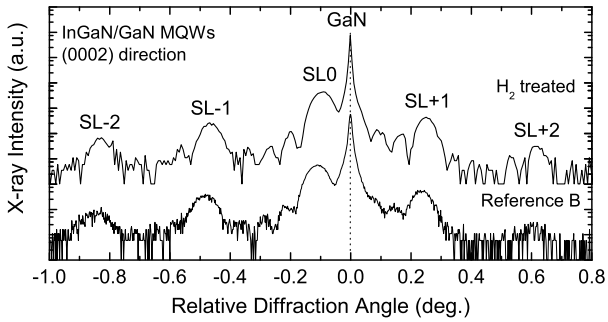

Figure 5.15. High resolution (0002) XRD curves of MQW samples with 15 % In content in the QWs. The GaN barriers were grown with a carrier gas flow ratio of $H_2/N_2 = 0.02$ (H_2 treated) and $H_2/N_2 = 0$ (reference) [Publ. IV].

grown on the GaN buffer in H_2 atmosphere. A 20 nm thick underneath InGaN layer was grown in all the samples excluding the reference sample before the MQW stack consisting of 10 pairs of 3 nm thick InGaN QWs and 25 nm thick GaN barriers. N_2 was used as the carrier gas during the growth of the UL and the MQW stack. Growth temperature of the InGaN wells was 760 ^{o}C. The p-type region consisted of a 20 nm thick $Al_{0.12}Ga_{0.88}N$ EBL and a 250 nm thick Mg-doped p-type layer. Before the growth of the EBL the growth temperature was increased to the p-GaN growth temperature of 970 ^{o}C.

The EL spectra of the fabricated LED samples are displayed in Fig. 5.16. Results show that the EL intensity increases while the UL In content is increased from 0 % to 1.5 % and then decreases with the higher In contents. All the UL samples showed a decrease of the FWHM of around 25 % corresponding to the reduction of 5-7 nm in the FWHM. Blue shift of the EL peak was observed in all the UL samples. The variation of the peak emission wavelength of the samples is not directly correlated to the indium composition of the UL. Some part of the wavelength variation may be explained by the run-to-run variations in the MOVPE reactor. However, the increase in the efficiency cannot be explained by the different alloy compositions of the InGaN wells because the sample with an UL had also a higher efficiency than our standard LED structure (without the UL) at the same wavelength of 440 nm.

It is well known that due to the large lattice mismatch between GaN and InN there is a large strain near the GaN/InGaN interface that results in a piezoelectric field in the InGaN layer even with small amounts of In. The piezoelectric field-induced QCSE results in a red-shift of the QW emission energy and reduces the radiative recombination efficiency [52]. It has been stated in other studies that InGaN layer

under the MQW stack might reduce the QCSE inside the active region causing a blue-shift of the EL peak and a decrease of the FWHM [108]. However, a possible alternative reason for different EL properties is the separation of the MQW stack and the GI interface of the high temperature GaN. It is possible that GI interface generates a large number of nonradiative recombination centers (NRCs) due to the desorption of nitrogen atoms or absorbtion of impurity atoms [106]. The additional In atoms of the UL may cause an efficient elimination of the GI interface generated NRCs.

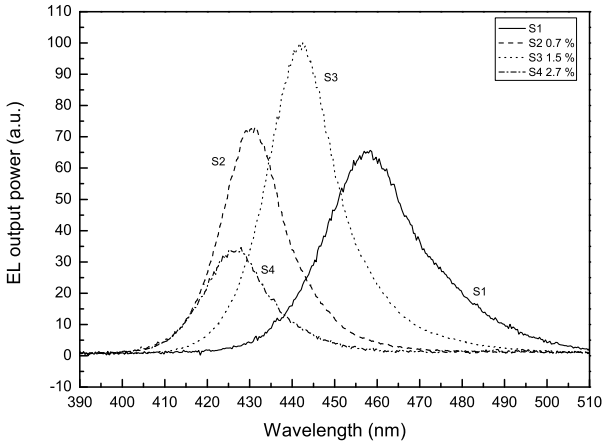

Figure 5.16. EL spectra of the InGaN/GaN LEDs without and with an UL having different In contents. A blue-shift and a decrease of FWHM can be observed in the all UL containing LED samples. The samples with an UL In content of 0.7 % and 1.5 % show also an increased EL output power compared to the reference sample [Publ. V].

Secondary ion mass spectroscopy (SIMS) depth profiles were taken from the reference sample and the sample with the UL In content of 1.5 % to further study the different EL behavior. Fig. 5.17 shows the SIMS depth profiles of the indium concentrations in these samples. The depth resolution of the SIMS analysis is limited due to the LED surface roughness. The InGaN UL can be seen as a low small increase of the In concentration before the deepest QW in the lower curve of Fig. 5.17. It can be seen that the presence of an UL reduces the variation of the In content from a QW to another. This is seen especially in the case of the deepest QW. These differences between the In concentrations of the QWs can give a good explanation for the decreased EL and PL FWHM of the sample having an UL with an In content of 1.5 % compared to the reference structure. The InGaN UL might

offer a higher quality growth base for the MQW stack compared to the GI interface of the reference sample. This increases the homogeneity of the In content of the MQW stack and contributes to improved EL performance.

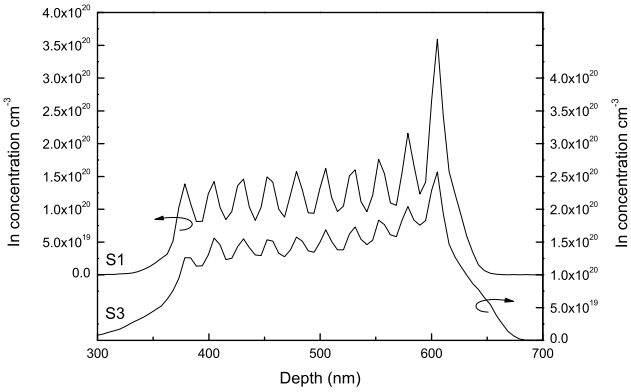

Figure 5.17. Indium concentration measured by SIMS in InGaN/GaN LEDs without (upper plot) and with an UL having the In content of 1.5 % (lower plot). The effect of the UL can be seen as slower decrease of the In content below the lowest QW [Publ. V].

5.4 InAlGaN layers and InGaN/InAlGaN quantum wells for near UV-LEDs

In order to realize high-power UV emitting LEDs in the range from 360 nm to 400 nm using III-N materials, it is necessary to obtain reasonably efficient emission from wide bandgap MQW structures. High efficiency and good carrier confinement can be achieved using MQW structures consisting of InAlGaN barriers and InGaN QWs [109, 110]. A small amount of In in the AlGaN barrier layers significantly increases the optical quality of the MQW stack [111]. Furthermore, quaternary InAlGaN allows the possibility to tune the strain state of the InGaN QWs between compressive strain, non-strained and tensile strain [112].

Fig. 5.18 shows the XRD (002) scans from a series of bulk InAlGaN samples with thicknesses of around 100 nm, which were grown on a GaN buffer layer at 850 ^{o}C in N2 ambient using a V/III ratio of 1100 at the pressure of 300 Torr. Constant TMGa and TMAl flows of 25 and and 51 μmol/min were used, respectively, while TMIn flow was varied between 0 and 46 μmol/min [Publ. VI]. It can be noted that as the TMIn flow is increased, the InAlGaN XRD peak shifts closer to the GaN

peak. The InAlGaN layer is almost lattice matched to GaN with the TMIn flow of 46 μmol/min. Multiple clear diffraction fringes in the XRD scans indicate sharp InAlGaN/GaN interfaces.

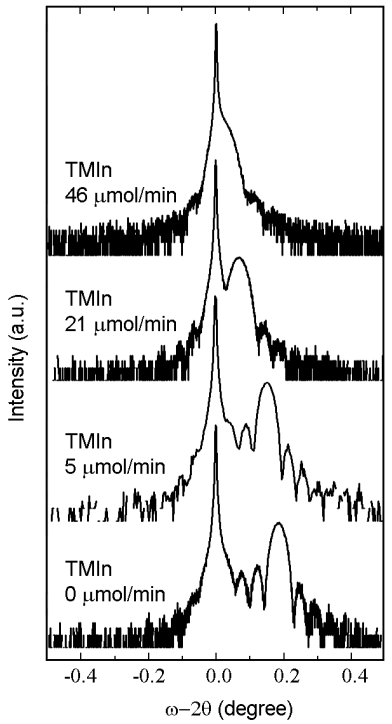

Figure 5.18. XRD (0002) ω-2θ diffraction curves of InAlGaN films grown with various TMIn flows [Publ. VI].

Fig. 5.18 shows the HRXRD (0002) ω-2θ diffraction curves of InAlGaN films grown with various TMIn flows. It can be seen that by increasing the TMIn flow the InAlGaN peak is shifted closer to the GaN peak, and the InAlGaN film is almost lattice matched to GaN when TMIn flow of 46 μmol/min is used. The presence of multiple clear diffraction fringes indicates sharp InAlGaN/GaN interfaces. The FWHM of the InAlGaN peak is determined by the layer thickness.

Fig. 5.19 shows the In and Al contents as a function of the TMIn flow. It can be noted that increasing the In precursor flow causes an increase in the In content as expected but also a decrease in the Al content. However, this is not so unexpected because varying TMAl flow has been reported to affect also the In content [113]. The SIMS depth profile of the InAlGaN samples grown with TMIn flows of 21 μmol/min or less showed sharp interfaces and uniform In and Al compositions [Publ. VI]. With TMIn flow of 46 μmol/min the Al content increased gradually from 0 to 0.12

during the first 20 nm starting from the beginning of InAlGaN layer growth on the GaN buffer. At the same time the In composition is uniform through the film [Publ. VI]. This effect is not caused by strain because the film is nearly lattice matched to GaN (see Fig. 5.18). More probable reason is that the increased In mole fraction disturbs the initial steps of the InAlGaN film growth due to increased compositional fluctuation of In [114].

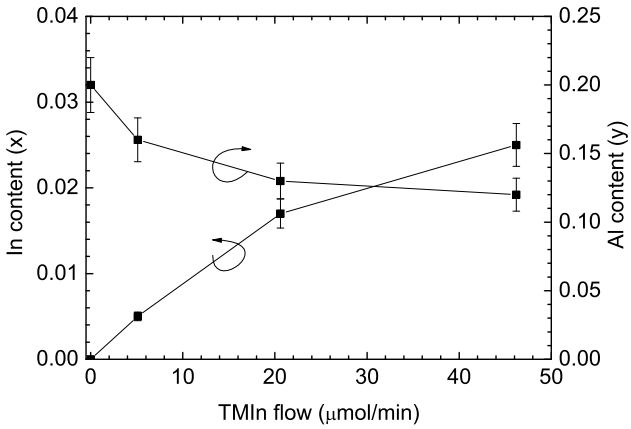

Figure 5.19. In and Al contents of $In_xAl_yGa_{1-x-y}N$ films as a function of TMIn flow [Publ. VI].

A series of InGaN/$In_xAl_yGa_{1-x-y}N$ MQW structures emitting at the wavelength range near 380 nm were fabricated to study the effect of barrier composition on the optical quality of the MQWs. After completion of the growth of the 2 μm thick GaN buffer layer, the carrier gas was switched from H_2 to N_2. A constant pressure of 300 nm was used during the growth of the active region. Fig. 5.20 shows the temperature versus time profile during the growth process. The 2 nm thick $In_{0.07}Ga_{0.93}N$ QWs were grown at the temperature of 794 ^{o}C with the growth time of 30 sec. After the growth of the QW layer, a thin InAlGaN capping layer was grown at the same temperature to protect the active layer from the high temperature required for the barrier growth. The temperature was then increased to 850 ^{o}C for 180 sec for the growth of the 20 nm thick $In_xAl_yGa_{1-x-y}N$ barrier layer. During the growth of the barrier layers TMGa flow of 25 μmol/min and TMAl flow of 51 μmol/min were used. The samples consisted of five QWs. TMIn flow was varied from 2.5-46.2 μmol/min during the growth of $In_xAl_yGa_{1-x-y}N$ barriers [Publ. VII].

Fig. 5.21 shows the XRD scans for the (002) reflection of the samples with various TMIn flows during the barrier growth. The thick underlying GaN buffer layer sauses the sharpest peak in the scan. The broader peak on the right of the GaN peak

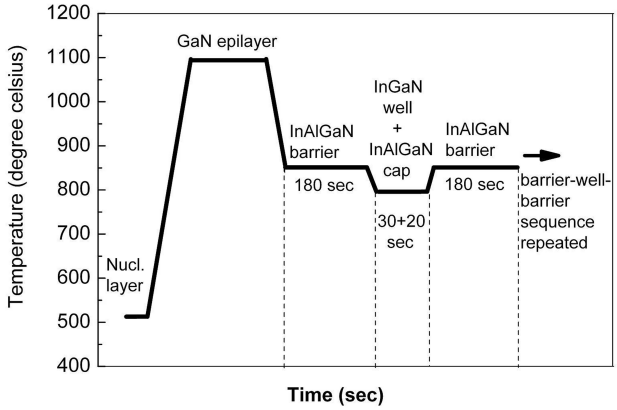

Figure 5.20. Temperature versus time profile during the MQW growth process [Publ. VII].

comes from the InGaN/$In_xAl_yGa_{1-x-y}N$ superlattice. The barrier In content range is 0.6-1.6 % while the TMIn flow is increased from 2.5 μmol/min to 46 μmol/min. The precursor flows and corresponding compositions of the barriers are shown in Table 5.5. The shift of the superlattice peak towards the GaN peak is a sign of a slight reduction in the tensile strain in the MQW stack with the increase of the TMIn flow. As shown in Table 5.5 the growth rate of $In_xAl_yGa_{1-x-y}N$ layer decreases with increasing TMIn flow which causes an increase in the satellite peak periodicity (Fig. 5.21). The weakening of the satellite peaks in the samples with increasing In content is due to the decrease of interference in the MQW stack caused by reduction of the Al content.

Table 5.5. In and Al contents of the barriers in InGaN/InAlGaN MQW samples and the corresponding precursor flows [Publ. VII].

TMIn flow *	TMAl flow *	In (x)	Al (y)	Growth rate**
2.5	51	0.006	0.160	0.11
5.14	51	0.007	0.160	0.11
10.27	51	0.011	0.155	0.10
20.55	51	0.013	0.145	0.09
46.23	51	0.016	0.130	0.08

*μmol/min, **nm/sec

Fig. 5.22 shows the IQEs of the samples calculated from the temperature dependent PL measurements. The total luminescence intensity ratios from 10 to 300 K were used to estimate the IQEs. It was assumed that nonradiative recombination is negligible at very low temperatures. The results indicate that the IQE increases with

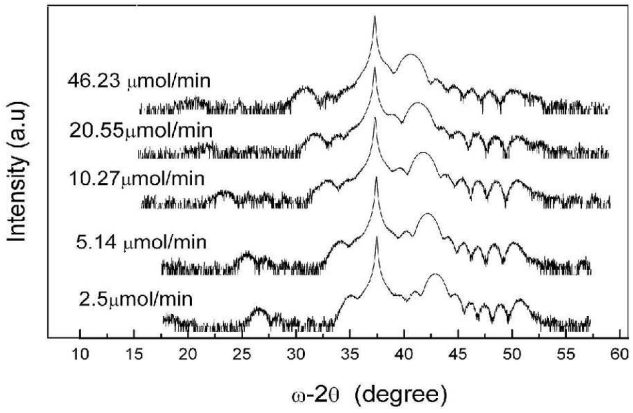

Figure 5.21. XRD (002) ω-2θ diffraction curves of five period InGaN/$In_xAl_yGa_{1-x-y}N$ MQWs with different TMIn flows during growth of the $In_xAl_yGa_{1-x-y}N$ barriers [Publ. VII].

increasing barrier In content until 1.28 % and decreases rapidly at higher values. The increase of IQE is most probably due to the reduction of tensile strain in the MQW stack. However, when the In content of the barriers exceeds 1.3 % the material quality deteriorates. This is not surprising taking account that $In_xAl_yGa_{1-x-y}N$ films grown with 46 μmol/min of TMIn flow have highly non-uniform distribution of Al. The inset shows the RT PL spectrum of the sample with the highest IQE. The FWHM of the RT PL peak for the samples with the different TMIn flows were within the range of 18±2 nm.

5.5 MOVPE growth of AlGaN electron blocking layer

A better carrier confinement in the active layer is achieved in III-N light emitting structures by preventing the electron overflow by using a Mg-doped AlGaN EBL between the MQW stack and the p-type GaN layer [56]. However, fabricating a successful EBL is a challenging task. The growth parameters and the placement of the AlGaN EBL can significantly affect the performance of the structure. A high enough doping level of the EBL is needed without deteriorating the crystal quality [56–58]. Furthermore, the MQW stack should be protected from harmful Mg back diffusion and H_2 ambient during the EBL growth to avoid the decrease of performance of the LED structure [115, 116].

In order to fabricate an efficient p-type doped AlGaN EBL, the effect of Mg doping level and AlGaN layer thickness was studied. All the samples were LED structures consisting of a 2 μm thick GaN buffer layer and a 2 μm thick GaN:Si n-type layer

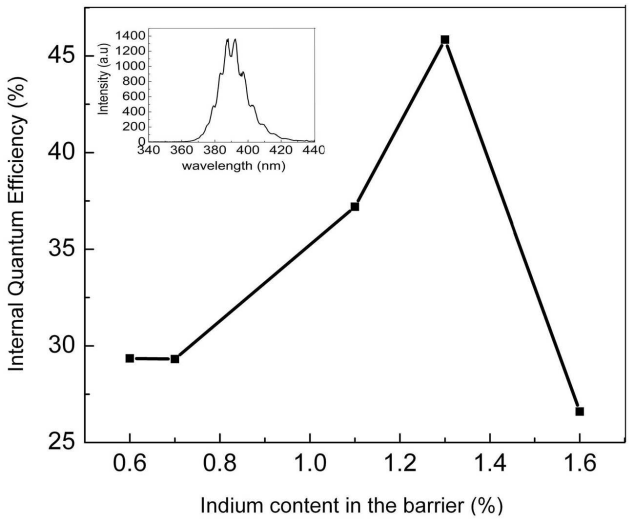

Figure 5.22. Internal quantum efficiencies of InGaN/$In_xAl_yGa_{1-x-y}N$ MQW structures as a function of the barrier In content. The other MQW stack parameters are shown in Table 5.5. The inset shows the room temperature PL spectrum of sample with the In content of 1.3 % in the barriers [Publ. VII].

with the carrier concentration of $6{\cdot}10^{18}$ cm^{-3}. The MQW stack consisted of ten 2.5 nm thick InGaN QWs separated by undoped 20 nm thick GaN barriers. The active region was followed by a 50 nm thick undoped GaN spacer grown during the temperature ramp up from 760 to 1000 ^{o}C. This particular spacer thickness was chosen after previous experiments. An $Al_{0.11}Ga_{0.89}N$ EBL was grown on top of the GaN spacer. A Mg-doped 250 nm thick p-type GaN having a hole concentration of $4{\cdot}10^{17}$ cm^{-3} was grown with a 80 sccm Cp_2Mg flow rate at 1000 ^{o}C on top of the EBL. Two different sample series were examined. A series of LEDs with different EBL doping levels was grown in order to evaluate how the EBL doping level affects the optical properties of the LEDs. The Mg flow rate during the EBL growth was varied between 0 and 100 sccm in the series. In the other series the optimal EBL thickness was investigated by growing EBLs with thicknesses ranging from 0 to 45 nm.

Fig. 5.23 shows the PL and EL measurements results from the samples grown with different Mg flows. There is a clear maximum in the EL intensity at a certain Mg flow rate while the PL intensity is almost constant throughout the sample series. From these PL and EL results we can conclude that the change in the EL intensity is not due to changes in the active region. They are rather caused by changes in carrier injection into the active region. When the carriers are properly injected, as now optically instead of electrically, intensity will not change. Back diffusion of Mg

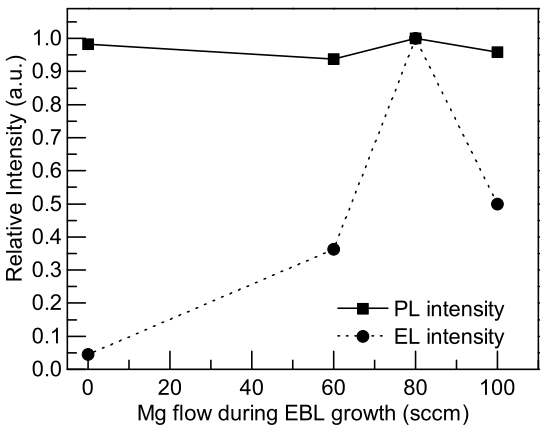

Figure 5.23. Relative PL and EL intensities of the LED structures with different Mg flow rates during AlGaN EBL growth. A clear maximum can be observed in the EL results while the PL intensity stays almost constant with different EBL doping levels [Publ. VIII].

atoms into the MQW stack would deteriorate the active region due the formation of NRCs which should be seen in the PL intensity [116]. This confirms that utilization of an undoped GaN spacer prevents Mg back diffusion from the EBL and p-type GaN into the MQW stack.

Fig. 5.24 shows the SIMS analysis of Mg atom diffusion from the p-type layers into the spacer layer which enables the hole injection into the active region. A clear shoulder is observed in all of the Mg profile slopes at the start of growth of the Mg containing material. This was observed also in the reference sample with an undoped EBL. The shoulder width is decreasing with increasing Mg flow during EBL growth. However, the Mg atom concentration of the shoulder does not change with the Mg flow rate. The depth position of the shoulder reveals that it appears at the beginning of doped material growth. The Mg concentration slopes at the right side of the shoulder are due to back diffusion of Mg towards the MQW stack. Diffusion related tail in the Mg doping profile is pronounced in the samples where the EBL has been doped. This supports the theory that Mg atom diffusion is larger into the spacer region than into the high growth temperature layers with higher quality. Similar behavior can also be seen from the Al doping profile. The shoulder in the Mg doping profiles can be explained with the loading effect of the reactor

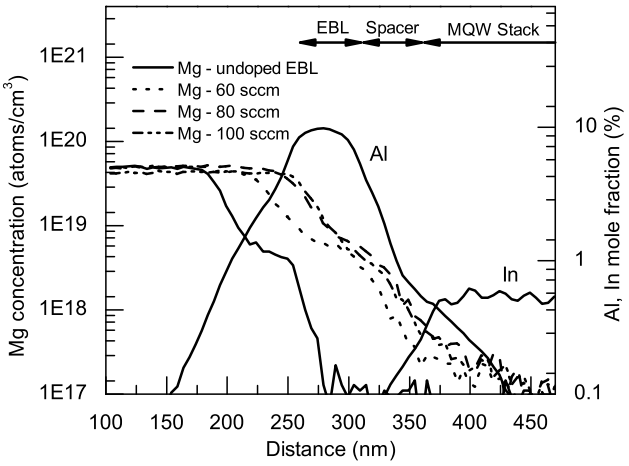

Figure 5.24. SIMS depth profiles from four LED structures with different Mg flow rates during growth of the AlGaN EBL. The EBL thickness (45 nm) together with the other spacer layer and active region parameters were kept constant in the sample series [Publ. VIII].

[117]. This means that there is less effective Mg available in the gas phase until the Mg concentration has balanced between the inner parts of the reactor and the growth ambient in the beginning of the growth step. This explains the large shoulder width of the reference sample in which the Mg doping was started in different growth ambient. It can be easily seen from the EL intensity measurements that the optimal doping is of decisive importance. Insufficient doping of the EBL region decreases the Mg back diffusion and prevents effective hole injection through the spacer layer leading to a decreased LED performance. This result is even more pronounced in the reference sample in which the EBL was completely undoped. Excessive doping is also harmful. The EL intensity decreases while the PL intensity stays at the same level. This means that the decrease of the EL intensity with high dopant flows is not due to back diffusion of Mg atoms into the MQW region but the reason is more likely the decreased crystal quality and electrical properties of the EBL layer with a high Mg flow.

Fig. 5.25 shows the EL and PL measurement results from the second sample series which was grown in order to optimize the EBL layer thickness. The EBL in this series was doped to the level optimized in the first sample series. The EBL thickness was varied from 0 to 45 nm. Again the PL intensity is nearly the same throughout

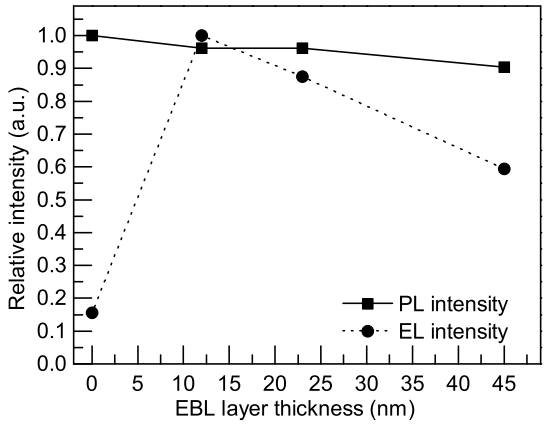

Figure 5.25. Relative PL and EL intensities of the LED structures with different EBL layer widths. A clear maximum can be observed in the EL results while the PL intensity stays almost constant [Publ. VIII].

the sample series indicating that the conditions in the active region remain similar. The decrease in the EL intensity with increasing EBL layer thickness from 12 nm can be explained by inadequate hole injection from the p-GaN contact region into the MQWs. This behavior can have two explanations. Either the low crystal quality of AlGaN prevents effective hole injection or reduced Mg atom diffusion from the heavily doped p-GaN into the spacer layer decreases the conductivity of the spacer layer. The importance of the EBL can be stated by comparing the EL intensity of the LED structures with and without the EBL. The EL intensity of the sample without an EBL is decreased to one-fifth compared to the sample containing an optimized EBL. This indicates that even a thin EBL successfully prevents electron overflow.

6 Summary

Fabrication and properties of III-N based LEDs were investigated in this thesis. The scope of the work was to improve the material properties and the efficiency of blue and near-UV LEDs. Several approaches were investigated for increasing light extraction from the epitaxial structure and for enhancing the material and optical quality of the LED structures grown on sapphire substrates. Chemically patterned and roughened sapphire substrates combined with subsequent MOVPE growth of the LED structure were examined in order to decrease the threading dislocation (TD) density of the GaN buffer layer and to increase the light extraction efficiency. It was found out that the TD density can be reduced by using a patterned substrate. Also with some samples it was observed that TD density varied locally with the sapphire pattern. However, the decrease was always lower than one order of magnitude contributing only to a small effect on device performance. On the other hand, light extraction was found to be improved significantly by optimized sapphire patterning or roughening.

The surface morphology of InGaN/GaN QWs and it's effect on the optical quality of the QWs were evaluated. Smooth surface morphology of the InGaN/GaN MQW stack and sharp interfaces between InGaN and GaN layers were achieved by increasing the barrier growth temperature of the barriers and by introducing simultaneously a small amount of H_2 to the carrier gas during the barrier growth. However, the efficiency of the blue MQW structure was nearly immune to the surface morphology. The InGaN underneath layer (UL) with a low 1.5 % In content was found to have a significant effect on the EL efficiency of the blue LEDs. It was found that the UL had a strong effect on the homogeneity of the MQW stack and especially on the In concentration of the deepest QWs.

InAlGaN barriers were investigated in order to improve the carrier confinement in the near-UV MQW structures. The In and Al compositions were found to be uniform up to the In content of 1.6 %. With higher In content the Al content at the InAlGaN/GaN interface became diffused. The increase in the In composition of the barriers increased internal quantum efficiency (IQE) until an In content of 1.38 %. With higher In content the efficiency deteriorated. The optimized MQW stack showed an IQE of 45 % at the wavelength of 382 nm.

The effect of AlGaN electron blocking layer (EBL) on the electrical and optical

properties of III-N LEDs was examined in order to prevent the electron flow from the active region. The EL efficiency was found to be very sensitive to the layer thickness and doping level of the EBL. Sufficient doping level was needed to achieve proper hole injection. Excessive doping lead to deteriorated crystal and electrical quality of the EBL. The EBL layer thickness was optimized to maintain effective hole injection while preventing electron overflow.

An UV-LED structure showing an output power of 4.1 mW at the wavelength of 405 nm with an operating current of 20 mA and a forward voltage of 3.37 V was fabricated by introducing part of the techniques summarized above into the previously developed LED structure. Measurement was performed on chip on wafer level without an encapsulant.

References

[1] D. A. Steigerwald, J. C. Bhat, D. Collins, R. M. Fletcher, M. O. Holcomb, M. J. Ludowise, P. S. Martin and S. L. Rudaz, IEEE J. Select. Topics Quant. Electr. **8**, 310 (2002).

[2] N. Holonyak and S. F. Bevacqua, Appl. Phys. Lett. **1**, 82 (1962).

[3] I. Akasaki, J. Crystal Growth **300**, 2 (2007).

[4] S. Keller and S. P. DenBaars, J. Cryst. Growth **248**, 479 (2003).

[5] H. Morko, *Handbook of Nitride Semiconductors and Devices, Volume 1: Materials Properties, Physics and Growth* (WILEY-VCH Verlag GmbH & Co. KGaA, 2008).

[6] S. Nakamura and G. Fasol, *The Blue Laser Diode* (Springer Verlag, 1997).

[7] S. Suihkonen, Ph.D. thesis, Helsinki University of Technology (2008).

[8] S.-H. Wei and A. Zunger, Appl Phys. Lett. **69**, 2719 (1996).

[9] A. Smith, R. Feenstra, D. Greve, M.-S. Shin, M. Skowronski, J. Neugebauer and J. Northrup, Surface Science **423**, 70 (1999).

[10] J. Neugebauer, phys. stat. sol. (b) **227**, 93 (2001).

[11] M. Stutzmann, O. Ambacher, M. Eickhoff, U. Karrer, A. Lima Pimenta, R. Neuberger, J. Schalwig, R. Dimitrov, P. J. Schuck and R. D. Grober, phys. stat. sol. (b) **228**, 505 (2001).

[12] J. Singh, *Semiconductor Optoelectronics Physics and Technology* (McGraw-Hill book Co., 1995).

[13] G. D. Chen, M. Smith, J. Y. Lin, H. X. Jiang, S.-H. Wei, M. Asif Khan and C. J. Sun, Appl. Phys. Lett. **68**, 2784 (1996).

[14] M. Androulidaki, N. T. Pelekanos, K. Tsagaraki, E. Dimakis, E. Iliopoulos, A. Adikimenakis, E. Bellet-Amalric, D. Jalabert and A. Georgakilas, phys. stat. sol. (c) **3**, 1866 (2006).

[15] F. Yun, M. A. Reshchikov, L. He, T. King, H. Morkoç, S. W. Novak and L. Wei, J. Appl. Phys. **92**, 4837 (2002).

[16] S. R. Lee, A. F. Wright, M. H. Crawford, G. A. Petersen, J. Han and R. N. Biefeld, Appl. Phys. Lett. **74**, 3344 (1999).

[17] I. Vurgaftman, J. R. Meyer and L. R. Ram-Mohan, J. Appl. Phys. **89**, 5815 (2001).

[18] S. C. Jain, M. Willander and J. Narayan, J. Appl. Phys. **87**, 965 (2000).

[19] M. A. Herman, W. Richter and H. Sitter, *Epitaxy, Physical Principles and Technical Implementation* (Springer-Verlag, 2004).

[20] O. Reentilä, Ph.D. thesis, Helsinki University of Technology (2007).

[21] T. Lang, M. A. Odnoblyudov, V. E. Bougrov, A. E. Tomanov, S. Suihkonen, M. Sopanen and H. Lipsanen, phys. stat. sol. **203**, R76 (2006).

[22] *Thomas Swan Scientific Equipment Ltd.* (2004).

[23] Y.-H. Cho, F. Fedler, R. J. Hauenstein, G. H. Park, J. J. Song, S. Keller, U. K. Mishra and S. P. DenBaars, J. Appl. Phys. **85**, 3006 (1999).

[24] S. Takagi and H. H. Wills, Acta Cryst. **15**, 1311 (1962).

[25] D. Taupin, Bull. Soc. Fr. Mineral. Cristallogr. **87**, 469 (1964).

[26] S. Sintonen, S. Suihkonen, O. Svensk, P. T. Törmä, M. Ali, M. Sopanen and H. Lipsanen, phys. stat. Sol. (c) **7**, 1790 (2010).

[27] H. D. Young, *University physics* (Addison Wesley Longman, Inc., 2000).

[28] A. K. Viswanath, J. I. Lee, S. Kim, G. M. Yang, H. J. Lee and D. Kim, Thin Solid Films **515**, 4401 (2007).

[29] L. A. Marasina, V. V. Malinovsky, I. G. Pichugin and P. Prentky, Crystal Res. Technol. **17**, 365 (1982).

[30] F. Dwikusuma, D. Saulys and T. F. Kuecha, J. Electroc. Soc. **149**, G603 (2002).

[31] C. J. Humphreys, MRS Bulletin **33**, 459 (2008).

[32] LED professional Review, p. 6 (2009), ISSN 1993-890X.

[33] Y. Uchida and T. Taguchi, Optical Engineering **44**, 124003 (2005).

[34] E. F. Schubert, *Light-emitting diodes* (Cambridge university press, 2003).

[35] M. R. Kramer, H. Amano, J. J. Brown and P. L. Heremans, IEEE J. Select. Top. Quant. Electronics, **8**, 185 (2002).

[36] J. Xie, X. Ni, Q. Fan, R. Shimada, . Özgür and H. Morkoc, Appl. Phys. Lett. **93**, 121107 (2008).

[37] B. Monemar and B. E. Sernelius, Appl. Phys. Lett. **91**, 181103 (2007).

[38] Y. Yang, IEEE Transactions on Electron Devices **55**, 1771 (2008).

[39] M.-H. Kim, M. F. Schubert, Q. Dai, J. K. Kim, E. F. Schubert, J. Piprek and Y. Park, Appl. Phys. Lett. **91**, 183507 (2007).

[40] N. F. Gardner, G. O. Müller, Y. C. Shen, G. Chen, S. Watanabe, W. Götz and M. R. Krames, Appl. Phys. Lett. **91**, 234506 (2007).

[41] H. P. Maruska and J. J. Tietjen, Appl. Phys. Lett. **15**, 327 (1969).

[42] B. Monemar, Phys. Rev. B **10**, 676 (1974).

[43] H. Amano, N. Sawaki, I. Akasaki and Y. Toyoda, Appl. Phys. Lett. **48**, 353 (1986).

[44] S. Nakamura, N. Iwasa, M. Senoh and T. Mukai, Jpn. J. Appl. Phys. **30**, L1705 (1991).

[45] S. Nakamura, N. Iwasa, M. Senoh and T. Mukai, Jpn. J. Appl. Phys. **31**, 1258 (1992).

[46] F. K. Yan and Z. Hassan, Microelectr. J. **36**, 129 (2005).

[47] X. H. Wu, P. Fini, E. J. Tarsa, B. Heying, S. Keller, U. K. Mishra, S. P. DenBaars and J. S. Speck, J. Cryst. Growth **189-190**, 231 (1998).

[48] I. Kidoguchi, G. Iishibashi, G. Sugahara and Y. Ban, Appl. Phys. Lett. **76**, 3768 (2000).

[49] A. M. Rokowski, P. Q. Miraglia, E. A. Prele, S. Einfeldt and R. F. Davis, J. Crystal Growth **241**, 141 (2002).

[50] C. I. H. Ashby, C. C. Mitchell, J. Han, N. A. Missert, P. P. Provencio, D. M. Follstaedt, G. M. Peake and L. Griego, Appl. Phys. Lett. **77**, 3233 (2000).

[51] D. S. Wuu, W. K. Wang, K. S. Wen, S. H. Huang, S. H. Lin, S. Y. Huang, C. F. Lin and R. H. Horng, Appl. Phys. Lett. **89**, 161105 (2006).

[52] S. F. Chichibu and et. al., Nature Materials **5**, 810 (2006).

[53] T. Takeuchi and et. al., Appl.Phys.Lett. **73**, 1691 (1998).

[54] M. D. McCluskey, L. T. Romano, B. S. Krusor, D. P. Bour, N. M. Johnson and S. Brennan, Appl Phys. Lett. **72**, 1730 (1998).

[55] H. Hirayama, J. Appl. Phys. **97**, 091101 (2005).

[56] S. Grzanka, G. Franssen, G. Targowski, K. Krowicki, T. Suski, R. Czernecki, P. Perlin and M. Leszczyński, Appl Phys. Lett. **90**, 103507 (2007).

[57] O. Svensk, S. Suihkonen, T. Lang, H. Lipsanen, M. Sopanen, M. A. Odnoblyudov and V. E. Bougrov, J. Crystal Growth **298**, 811 (2007).

[58] A. Feduniewicz, C. Skierbiszewski, M. Siekacz, Z. Wasilewski, I. Sproule, S. Grzanka, R. Jakiela, J. Borysiuk, G. Kamler, E. Litwin-Staszewska, R. Czernecki, M. Boćkowskia and S. Porowski, J. Crystal Growth **278**, 443 (2005).

[59] J.-K. Ho, C. Jong, C. C. Chiu, C.-Y. Chen and K.-K. Shih, Appl. Phys. Lett. **74**, 1275 (1999).

[60] T. Margalith, O. Buchinsky, D. A. Cohen, A. C. Abare, M. Hansen, S. P. DenBaars and L. A. Coldren, Appl. Phys. Lett. **74**, 3930 (1999).

[61] S. J. Chang, C. S. Chang and Y. K. Su, IEEE J. Quan. Electron. **39**, 1439 (2003).

[62] Y. C. Lin, S. J. Chang, Y. K. Su, T. Y. Tsai, C. S. Chang, S. C. Shei, S. J. Hsu, C. H. Liu, U. H. Liaw, S. C. Chen and B. R. Huang, IEEE Photon. Technol. Lett. **14**, 1668 (2002).

[63] J.-H. Lim, D.-K. Hwang, M.-K. Kwon, I.-K. Park, S.-I. Na and S.-J. Park, phys. stat. sol. (c) **2**, 2533 (2005).

[64] J. J. Wierer, D. A. Steigerwald, M. R. Krames, J. J. O'Shea, M. J. Ludowise, G. Christenson, Y.-C. Shen, C. Lowery, P. S. Martin, S. Subramanya, W. Götz, N. F. Gardner, R. S. Kern and S. A. Stockman, Appl. Phys. Lett. **78**, 3379 (2001).

[65] V. Härle, B. Hahn, S. Kaiser, A. Weimar, D. Eisert, S. Bader, A. Plössl and F. Eberhard, Proc. of SPIE **4996**, 133 (2003).

[66] V. Härle, B. Hahn, J. Baur, M. Fehrer, A. Weimar, S. Kaiser, D. Eisert, F. Eberhard, A. Plössl and S. Bader, Proc. of SPIE **5187**, 34 (2004).

[67] O. B. Shchekin, J. E. Epler, T. A. Trottier, T. Margalith, D. A. Steigerwald, M. O. Holcomb, P. S. Martin and M. R. Krames, Appl. Phys. Lett. **89**, 071109 (2006).

[68] M. Hao, T. Egawa and H. Ishikawa, Appl. Phys. Lett. **89**, 241907 (2006).

[69] G. Franz, Materials Science in Semiconductor Processing **2**, 349 (1999).

[70] T. Fujii, Y. Gao, R. Sharma, E. L. Hu, S. P. DenBaars and S. Nakamura, Appl. Phys. Lett. **84**, 855 (2004).

[71] D. L. Hibbard, S. P. Jung, C. Wang, D. Ullery, Y. S. Zhao, H. P. Lee, W. So and H. Liu, Appl. Phys. Lett. **83**, 311 (2003).

[72] I. Schnitzer, E. Yablonovitch, C. Caneau, T. J. Gmitter and A. Scherer, Appl. Phys. Lett. **63**, 2174 (1993).

[73] S. H. Kim, K.-D. Lee, J.-Y. Kim, M.-K. Kwon and S.-J. Park, Nanotechnology **18**, 055306 (2007).

[74] T.-X. Lee, K.-F. Gao, W.-T. Chien and C.-C. Sun, Optics Express **15**, 6670 (2007).

[75] M. Yamada, T. Mitani, Y. Narukawa, S. Shioji, I. Niki, S. Sonobe, K. Deguchi, M. Sano and T. Mukai, Jpn. J. Appl. Phys. **41**, L1431 (2002).

[76] Y. P. Hsu, S. J. Chang, Y. K. Su, J. K. Sheu, C. T. Lee, T. C. Wen, L. W. Wu, C. H. Kuo, C. S. Chang and S. C. Shei, J. Crystal Growth **261**, 466 (2004).

[77] D. S. Wuu, W. K. Wang, W. C. Shih, R. H. Horng, C. E. Lee, W. Y. Lin and J. S. Fang, IEEE Photon. Technol. Lett. **17**, 288 (2005).

[78] Y. J. Lee, J. M. Hwang, T. C. Hsu, M. H. Hsieh, M. J. Jou, B. J. Lee, T. C. Lu, H. C. Kuo and S. C. Wang, IEEE Photon. Technol. Lett. **18**, 1152 (2006).

[79] K. Okamoto, I. Niki, A. Shvartser, Y. Narukawa, T. Mukai and A. Scherer, Nature Materials **3**, 601 (2004).

[80] W. L. Barnes, Nature Materials **3**, 588 (2004).

[81] S.-H. Park, H. Jeon, Y.-J. Sung and G.-Y. Yeom, Appl. Opt. **40**, 3698 (2001).

[82] S.-J. Kim, Jpn. J. Appl. Phys. **44**, 2921 (2005).

[83] H. S. Kim, J. S. Hwang and P. J. Chong, J. Kor. Chem. Soc. **39**, 1 (1995).

[84] X. Ding, T. Sato, Y. Kawaguchi and H. Niino, Jpn. J. Appl. Phys. **42**, L176 (2003).

[85] Y. J. Lee, T. C. Hsu, H. C. Kuo, S. C. Wang, Y. L. Yang, S. N. Yen, Y. T. Chu, Y. J. Shen, M. H. Hsieh, M. J. Jou and B. J. Lee, Material Science and Engineering B **122**, 184 (2005).

[86] S. J. Chang, Y. C. Lin, Y. K. Su, C. S. Chang, T. C. Wen, S. C. Shei, J. C. Ke, C. W. Kuo, S. C. Chen and C. H. Liu, Sol. Stat. Electr. **47**, 1539 (2003).

[87] S.-J. Kim, Phys. Stat. Sol. (a) **203**, 997 (2006).

[88] Y. P. Hsu, S. J. Chang, Y. K. Su, J. K. Sheu, C. H. Kuo, C. S. Chang and S. C. Shei, Optical Materials **27**, 1171 (2005).

[89] V. E. Bougrov, M. A. Odnoblyudov, A. E. Romanov, T. Lang and O. V. Konstantinov, phys. status solidi (a) **203**, R25 (2006).

[90] K. Hiramatsu, K. Nishiyamaa, T. Iyechikab and Maedaet, J. Crystal Growth **221**, 316 (2000).

[91] A. Hangleiter, F. Hitzel, C. Netzel, D. Fuhrmann, U. Rossow, G. Ade and P. Hinze, Phys. Rev. Lett. **95**, 127402 (2005).

[92] S. Suihkonen, O. Svensk, T. Lang, H. Lipsanen, M. A. Odnoblyudov and V. E. Bougrov, J. Crystal Growth **298**, 740 (2007).

[93] S. Nakamura, Microelectronics J. **25**, 651 (1994).

[94] Y.-S. Lin, K.-J. Ma, C. Hsu, S.-W. Feng, Y.-C. Cheng, C.-C. Liao, C. C. Yang, C.-C. Chou, C.-M. Lee and J.-I. Chyi, Appl. Phys. Lett. **77**, 2988 (2000).

[95] I.-H. Kim, H.-S. Park, Y.-J. Park and T. Kim, Appl. Phys. Lett. **73**, 1634 (1998).

[96] Y. Chen, T. Takeuchi, H. Amano, I. Akasaki, N. Yamada, Y. Kaneko and S. Y. Wang, Appl. Phys. Lett. **72**, 710 (1998).

[97] Z. Liliental-Weber, Y. Chen, S. Ruvimov and J. Washburn, Phys. Rev. Lett. **79**, 2838 (1997).

[98] C. J. Sun, M. Zubair Anwar, Q. Chen, J. W. Yang, M. Asif Khan, M. S. Shur and A. D. Bykhovski, Appl. Phys. Lett. **70**, 2978 (1997).

[99] X. H. Wu, C. R. Elsass, A. Abare, M. Mack, S. Keller, P. M. Petroff, S. P. DenBaars, J. S. Speck and S. J. Rosner, Appl. Phys. Lett. **72**, 692 (1998).

[100] J. E. Northrup and J. Neugebauer, Phys. Rev. B **60**, R8473 (1999).

[101] J. Off, F. Scholz, E. Fehrenbacher, O. Gfrörer, A. Hangleiter, G. Brockt and H. Lakner, phys. stat. sol. (b) **216**, 529 (1999).

[102] S. M. Ting, J. C. Ramer, D. I. Florescu, V. N. Merai, B. E. Albert, D. S. Lee, D. Lu, D. V. Christini, L. Liu and E. A. Armour, J. Appl. Phys. **94**, 1461 (2003).

[103] F. Scholz, J. Off, E. Fehrenbacher, O. Gfrörer and G. Brockt, phys. stat. sol. (a) **180**, 315 (2000).

[104] B. Van Daele, G. Van Tendeloo, K. Jacobs, I. Moerman and M. R. Leys, Appl. Phys. Lett. **85**, 4379 (2004).

[105] Y.-T. Moon, D.-J. Kim, K.-M. Song, C.-J. Choi, S.-H. Han, T.-Y. Seong and S.-J. Park, J. Appl. Phys. **89**, 6514 (2001).

[106] T. Akasaka, H. Gotoh, T. Saito and T. Makimoto, Appl. Phys. Lett. **85**, 3089 (2004).

[107] N. Nanhui, W. Huaibing, L. Jianping, L. Naixin, X. Yanhui, H. Jun, D. Jun and S. Guangdi, J. Crystal Growth **286**, 209 (2006).

[108] N. Nanhui, W. Huaibing, L. Jianping, L. Naixin, X. Yanhui, H. Jun, D. Jun and S. Guangdi, Solid-State Electron. **51**, 860 (2007).

[109] H. Hirayama, J. Appl. Phys. **97**, 091101 (2005).

[110] M. E. Aumer, S. F. LeBoeuf, F. G. McIntosh and S. M. Bedair, Appl. Phys. Lett. **75**, 3315 (1999).

[111] D. Zhu, M. J. Kappers, P. M. F. J. Costa, C. McAleese, F. D. G. Rayment, G. R. Chabrol, D. M. Graham, P. Dawson, E. J. Thrush, J. T. Mullins and C. J. Humpreys, phys. stat. sol. (a) **203**, 1819 (2006).

[112] M. E. Aumer, S. F. LeBoeuf, S. M. Bedair, M. Smith, J. Y. Lin and H. X. Jiang, Appl. Phys. Lett. **77**, 821 (2000).

[113] V. Perez-Solorzano, A. Groening, R. Haerle, H. Schweizer and M. Jetter, J. Crystal Growth **272**, 386 (2004).

[114] J. P. Liu, R. Q. Jin, J. C. Zhang, J. F. Wang, J. J. Wu, D. G. Zhao, Y. T. Wang and H. Yang, J. Phys. D Appl. Phys. **37**, 2060 (2003).

[115] U. Kaufmann, M. Kunzer, H. Obloh, M. Maier, C. Manz, A. Ramakrishnan and B. Santic, Phys. Rev. B **59**, 5561 (1999).

[116] T. Stephan, K. Köhler, M. Kunzer, P. Schlotter and J. Wagner, phys. status solidi (c) **0**, 2198 (2003).

[117] T. F. Kuech, P.-J. Wang, M. A. Tischler, R. Potemski, G. J. Scilla and F. Cardone, J. Crystal Growth **93**, 624 (1988).

Aalto-DD 27/2011

ISBN: 978-952-60-4082-0 (pdf)
ISBN: 978-952-60-4081-3
ISSN-L: 1799-4934
ISSN: 1799-4942 (pdf)
ISSN: 1799-4934

Aalto University
School of Electrical Engineering
Department of Micro- and Nanosciences
aalto.fi

BUSINESS + ECONOMY

ART + DESIGN + ARCHITECTURE

SCIENCE + TECHNOLOGY

CROSSOVER

DOCTORAL DISSERTATIONS